

Double-Pion Production Reactions in $\bar{p}n$ Collisions at 2.8 GeV/c*

T. C. BACON,† F. BOMSE, T. B. BORAK,‡ W. J. FICKINGER,§ E. R. GOZA,|| E. J. MOSES, AND E. O. SALANT

Department of Physics, Vanderbilt University, Nashville, Tennessee 37203

(Received 18 February 1970)

The reactions $\bar{p}n \rightarrow \bar{p}n\pi^+\pi^-$, $\bar{p}n \rightarrow \bar{p}p\pi^-\pi^0$, and $\bar{p}n \rightarrow \bar{n}p\pi^-\pi^-$ at 2.8-GeV/c incident \bar{p} laboratory momentum are analyzed with data from the Brookhaven National Laboratory 20-in. bubble chamber. $N^*(1238)$ isobar production in these channels is studied. It is found that the absorptive single-pion-exchange model cannot adequately explain all the features of simultaneous isobar production in these reactions. When the reactions $\bar{p}n \rightarrow (\bar{N}^{*-}-N^{*+} \text{ or } \bar{N}^{*0}N^{*-}) \rightarrow \bar{p}\pi^-n\pi^+$ are compared with their counterpart $\bar{p}p \rightarrow N^{*+}N^{*0} \rightarrow \bar{p}p\pi^+\pi^-$, the former are found to be less peripheral than the latter, in sharp disagreement with a prediction of the model. A generalized single-pion-exchange model is discussed which gives better agreement with the nucleon-pion two-body mass and angular distributions. Some evidence for enhancements in the nucleon and antinucleon dipion systems at 1400 MeV is discussed.

I. INTRODUCTION

THIS paper is concerned primarily with $\bar{p}n$ interactions in the reactions

- (A) $\bar{p}d \rightarrow \bar{p}n\pi^-\pi^+(p)$
 (B) $\rightarrow \bar{p}p\pi^-\pi^0(p)$
 (C) $\rightarrow \bar{n}p\pi^-\pi^-(p)$

caused by 2.8-GeV/c antiprotons incident on a deuterium-filled bubble chamber. Spectator nucleons are in parentheses.

The reactions

- (D) $\bar{p}d \rightarrow \bar{p}p\pi^-\pi^+(n)$
 (E) $\rightarrow \bar{p}p\pi^-(p)$

in the same exposure have been the subject of previous publications.^{1,2} Reaction (D), the only one of the reactions with a proton as target, will be the subject of an ensuing paper.

The data for analyzing the above reactions are taken from measurements obtained by Bacon *et al.*² from an exposure of the 20-in. BNL bubble chamber to antiprotons from the alternating gradient synchrotron. The average laboratory momentum of the antiprotons at the bubble-chamber entrance window was 2.79 GeV/c, with a maximum fluctuation from this value of 0.035 GeV/c.

* Work supported in part by a grant from the National Science Foundation, which is gratefully acknowledged. Computing for this experiment was done at the U. S. Army Computing Center at Redstone Arsenal, Huntsville, Ala., and at the AEC Computer Center, New York University, New York.

† Present address: Rutherford High-Energy Laboratory, Chilton, Didcot, Berkshire, England.

‡ Present address: National Accelerator Laboratory, Batavia, Ill.

§ Present address: Physics Department, Case Western Reserve University, Cleveland, Ohio.

|| Present address: Physics Department, Louisiana State University, Baton Rouge, La.

¹T. C. Bacon, F. Bomse, T. B. Borak, T. B. Cochran, W. J. Fickinger, E. R. Goza, H. W. K. Hopkins, and E. O. Salant, *Phys. Rev. Letters* **22**, 43 (1969).

²T. C. Bacon, F. M. Bomse, T. B. Cochran, W. J. Fickinger, E. R. Goza, H. W. K. Hopkins, and E. O. Salant, *Phys. Rev.* **162**, 1320 (1967).

II. GENERAL PROCEDURE

The raw data for this study consisted of approximately 48 000 bubble-chamber photographs, all of which were scanned for events with three or four outgoing charged prongs. From a second independent scan of about 12 000 pictures, the scanning efficiency was determined to be 90%. These procedures yielded 6100 three-pronged and 14 600 four-pronged events. The pictures were measured on three machines (built at Vanderbilt). Two of these, film plane digitizers incorporating Brower microscope stage assemblies, had a precision of 1 μ on the film; the third machine, an image plane digitizer utilizing a Mangiaspago bipolar coordinate measuring system, had a precision of 10 μ on the film.

For half the events, spatial reconstruction and kinematic fitting were performed with the TRED-KICK³ analysis system on an IBM 7094 computer at the Army Computer Center, Huntsville, Ala. For the other half, the Harwell package HGEOM-HKIN-KINC³⁴ and the CDC 6600 computer at the AEC Computer Center, New York University, New York, were used. Extensive tests conducted on a sample of events processed by both sets of programs showed that the values of all fitted and unfitted variables obtained from each of these systems were equal, to well within their respective error bars.

The criteria used for assigning events to the various categories were (1) a χ^2 probability greater than 1% for the fit corresponding to that category, (2) ionization, as observed by a physicist at the scanning table,

³J. K. Kopp, BNL-BCG Internal Reports F-120 and F-122, 1964 (unpublished); UCRL Internal Report No. UCRL-9099, edited by A. H. Rosenfeld, 1964 (unpublished). See also J. P. Berge, F. T. Solmitz, and H. D. Taft, *Rev. Sci. Instr.* **32**, 538 (1961).

⁴J. W. Burren and J. Sparrow, National Institute for Research in Nuclear Science Report No. NIRL/R/14, 1963 (unpublished); A. G. William, National Institute for Research in Nuclear Science Report No. NIRL/M/38, 1962 (unpublished); *Geometry Program Manual* (Rutherford High-Energy Laboratory, Chilton, Didcot, Berkshire, England, 1968); *Kinematics Program Manual* (Rutherford High-Energy Laboratory, Chilton, Didcot, Berkshire, England, 1968); *Geometry Testing Program Optical Constants*, (Rutherford High-Energy Laboratory, Chilton, Didcot, Berkshire, England, 1968).

consistent to within 50% for each track of that calculated by the kinematic fitting program for the fit, and (3) missing mass consistent (within its own error) with the mass of the neutral particle (if any) assigned to the fit.

In Fig. 1 is shown a scatter plot of the final-state neutron momentum versus the final-state proton momentum for events in categories (A) and (D). It is seen that most events have either a low-momentum proton or a low-momentum neutron but only rarely is there one with two slow nucleons. The channels (A) and (D) were separated by assuming that in each case the nucleon with smaller momentum was the spectator. In general, only events in which the spectator momentum itself was less than 250 MeV/c, a range in which the impulse approximation is valid,⁵ were used in the analysis.

In reactions (A)–(C), there is a neutral particle as well as a spectator proton in the final state. When the spectator momentum was low enough for the track to be visible, events in these categories were kinematically indeterminate. They were retrieved, however, by inserting a dummy proton into the kinematic fitting programs. The validity of this procedure was ensured by carrying out the ensuing physics analysis separately for events with visible and invisible spectator protons. No differences were apparent in the two samples. Accordingly, in the remainder of this paper, we combine these samples without distinguishing between them.

III. CROSS SECTIONS

The cross section for a particular channel was obtained from the formula

$$\sigma = \frac{I}{B} \frac{\sigma_T}{1 - e^{-\sigma_T N L}} \quad (1)$$

In this expression, σ_T is the total $\bar{p}d$ cross section at 2.8 GeV/c, N is the number of deuteron targets per cubic centimeter, L is the length of our fiducial volume, I is the number of events identified as belonging to the particular channel in question, and B is the total number of incident beam tracks in the experiment. For σ_T we used the value 137 ± 2 mb obtained by Abrams *et al.*⁶ in a counter experiment.

In calculating the cross sections for channels (A)–(E), it was necessary to apply a correction to account for the shadowing of the neutron⁷ by the proton in the deuteron target and vice versa. The correction factor used here was based on deuteron cross-section-defect

⁵ T. C. Bacon, H. W. K. Hopkins, D. K. Robinson, E. O. Salant, A. Engler, H. E. Fisk, C. M. Meltzer, and J. Westgard, *Phys. Rev.* **139**, B1420 (1965).

⁶ R. J. Abrams, R. L. Cool, G. Giacomelli, T. F. Kycia, B. A. Leontić, K. K. Li, and D. N. Michael, *Phys. Rev. Letters* **18**, 1209 (1967).

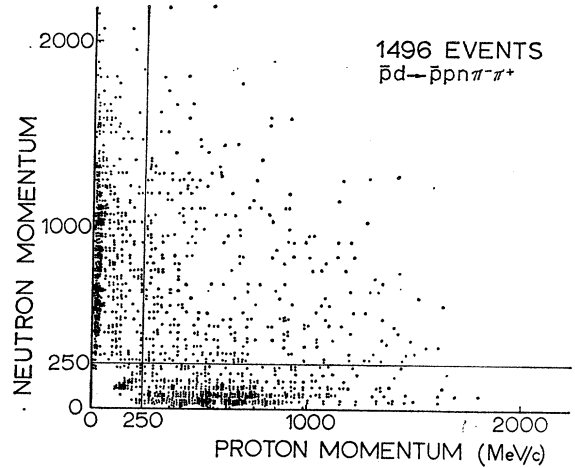


FIG. 1. Scatter plot of fitted neutron momentum versus proton momentum for events fitting the reaction $\bar{p}d \rightarrow \bar{p}pn\pi^-\pi^+$.

calculations of Glauber⁷ and of Franco and Glauber.⁸ The actual cross section for each channel was obtained as follows:

$$\sigma(\text{actual}) = \sigma(\text{measured}) G, \quad (2)$$

where $\sigma(\text{measured})$ is the cross section determined in Eq. (1) and G is the Glauber correction. The value of G appropriate to the interaction of 2.8-GeV/c antiprotons with deuterium is 1.12. The Glauber-corrected cross sections for the double-pion production reactions (A)–(D) are displayed in Table I.

IV. REACTION $\bar{p}n \rightarrow \bar{p}n\pi^+\pi^-$

A total of 529 events was identified as belonging to the channel $\bar{p}n(p) \rightarrow \bar{p}n\pi^+\pi^-(p)$ with proton spectator momentum less than 250 MeV/c. This corresponds to a cross section of 1.5 ± 0.2 mb.

The effective masses of the $\bar{p}\pi^-$ and $n\pi^+$ systems are displayed in the scatter plot of Fig. 2(a). A similar plot of the $n\pi^-$ mass versus the $\bar{p}\pi^+$ mass is shown in Fig. 2(b). Also shown in these figures are the histograms obtained by projecting the scatter plots on the mass axes. It is to be noted that each of the above pairings contains one $T_z = -\frac{3}{2}$ system and one $T_z = +\frac{1}{2}$ system

TABLE I. Summary of $\bar{p}d$ and $p\bar{p}$ cross sections at 2.8 GeV/c.

Reaction	Number of events	Cross section (mb)
$\bar{p}p(n) \rightarrow \bar{p}p\pi^-\pi^+(n)$	602	1.7 ± 0.2
$\bar{p}n(p) \rightarrow \bar{p}n\pi^-\pi^+(p)$	529	1.5 ± 0.2
$\bar{p}n(p) \rightarrow \bar{p}p\pi^-\pi^0(p)$	331	0.9 ± 0.1
$\bar{p}n(p) \rightarrow \bar{n}p\pi^-\pi^-(p)$	110	0.3 ± 0.04
$p\bar{p} \rightarrow p\bar{p}\pi^-\pi^+$	1558	2.51 ± 0.14^a

^a I. Richard Lapidus, thesis, Columbia University, 1963 (unpublished).

⁷ R. J. Glauber, *Phys. Rev.* **100**, 242 (1955).

⁸ V. Franco and R. J. Glauber, *Phys. Rev.* **142**, 1195 (1966).

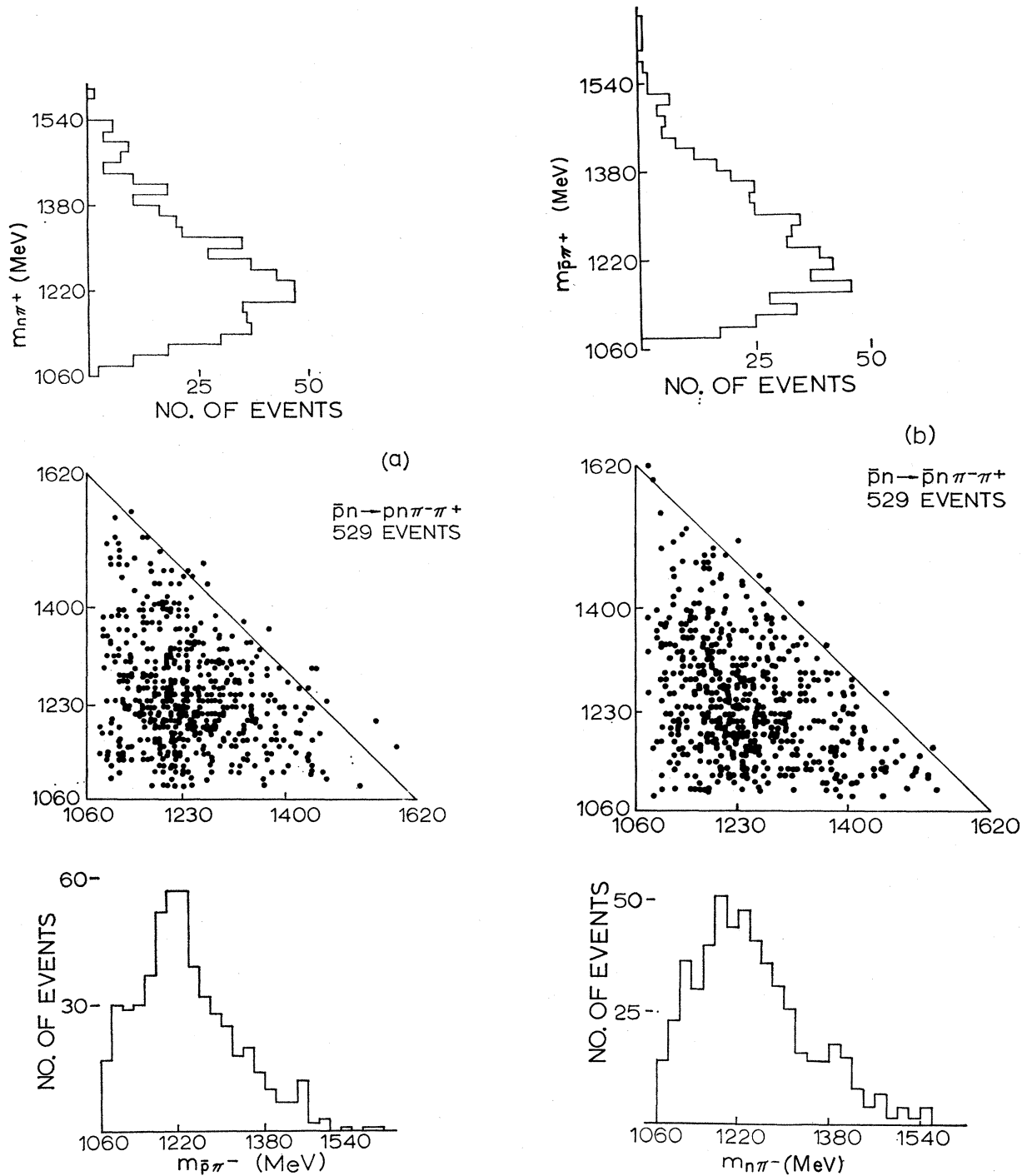


FIG. 2. (a) Scatter plot of $m_{n\pi^+}$ versus $m_{\bar{p}\pi^-}$ for 529 events of the type $\bar{p}n(\phi) \rightarrow \bar{p}n\pi^+\pi^-(\phi)$. (b) Scatter plot of $m_{\bar{p}\pi^+}$ versus $m_{n\pi^-}$ for 529 events of the type $\bar{p}n(\phi) \rightarrow \bar{p}n\pi^+\pi^-(\phi)$.

(where T_z is the third component of isospin). There is evidence for production of the $N^*(1238)$ isobar particularly in the $T_z = -\frac{3}{2}$ mass distributions.

It is assumed that the dynamics of this reaction are dominated by the exchange of a single pion. Moreover,

it is possible for the reaction to proceed through either of the quasi-two-body intermediate states

$$(F) \quad \bar{p}n \rightarrow \bar{N}^* N^* \rightarrow \bar{p}\pi^- + n\pi^+$$

$$(G) \quad \rightarrow \bar{N}^* N^* \rightarrow \bar{p}\pi^+ + n\pi^-.$$

In order to compare the data with a single-pion-exchange model for simultaneous \bar{N}^*N^* production, double-isobar events were selected by requiring that one $n\pi$ system, as well as one $\bar{p}\pi$ system, falls in the mass region 1160–1300 MeV. This procedure yielded 122 events of type (F) and 119 events of type (G), with 38 ambiguous events in which all four nucleon- (antinucleon-) pion masses satisfied the criterion. This result was incidentally a partial check on the data analysis, since isospin conservation implies that reactions (F) and (G) should occur equally often.

To investigate further the quality of the samples thus chosen, a Monte Carlo program was used to generate events of type (F) and (G). The input parameters to this program were taken from the experimental distributions. Upon making the double-resonance cut, 9% of the Monte Carlo events within the double-resonance region were found to be incorrectly paired and another 9% had all four nucleon- (antinucleon-) pion masses within this region. The various mass and angular distributions of these ambiguous Monte Carlo events were compared with the corresponding distributions of the other Monte Carlo events, but no significant differences were found. Thus, it was concluded that although incorrect pairings might contribute as much as 18% background to the experimental samples, such background would not significantly distort the mass and angular distributions of interest. Since quasi-two-body reactions are usually peripheral, the ambiguous events were sorted by choosing the more peripheral of the two possible double-resonance pairs, where the terminology "more peripheral" is to be understood in the following context. For each event one considers two four-momentum transfers, the one from the incoming \bar{p} to the outgoing $\bar{p}\pi^-$ system and the other from the incoming \bar{p} to the outgoing $\bar{p}\pi^+$ system. The more peripheral double-isobar pair is the pair corresponding to the smaller value of squared four-momentum transfer. By comparison with the Monte Carlo sample, this method proved to be correct in selecting the right reaction for 60% of the events. The experimental

samples were thus increased to 141 events for reaction (F) and 138 events for reaction (G).

Figure 3 shows the production angular distributions of the two $T_z = -\frac{3}{2}$ isobars from reactions (F) and (G), in the center-of-mass frame of the incoming particles. In both cases the angle θ_{prod} was defined with respect to the incoming \bar{p} in that frame. The solid curves are the predictions of the absorptive single-pion-exchange model of Jackson and collaborators⁹ with absorption coefficients $C_1 = C_2 = 1$. The values of the parameters γ_1 and γ_2 are those which gave best agreement with single-isobar production² in the reaction $\bar{p}n \rightarrow \bar{p}\pi p$. In this connection it is helpful to recall that in the absorptive single-pion-exchange model, each partial wave in the amplitude is multiplied by the factor $e^{i[\delta_l(f) + \delta_l(i)]}$, where $\delta_l(f)$ and $\delta_l(i)$ are elastic scattering phase shifts for the l th partial wave in the final and initial states, respectively. This factor in turn can be written as $(1 - C_2 e^{-\gamma_2 l^2})(1 - C_1 e^{-\gamma_1 l^2})$, where the parameters γ_1 and γ_2 are related to the slopes of the respective elastic differential cross sections. The reaction used to determine the γ 's has the same initial state as the one under consideration here and, except for the replacement of a nucleon by an isobar, it has the same final state. Hence the only assumption involved in using these γ 's is that the elastic scattering slopes are the same for $N^*-\bar{p}$ and N^*-N^* . The curves have been normalized to the number of events observed in the region $|\cos\theta_{\text{prod}}| \geq 0.5$. The experimentally determined cross section for each of the reactions over the entire range of the production angle was 0.78 ± 0.08 mb, while the model predicts 1.25 mb. Thus, even though values of the parameters in this model can be chosen so as to give good agreement with the shape of the differential cross section, the total cross section corresponding to this choice of parameters is too large.

A further test of the model involves the decay angular distributions of the isobars which can be discussed in terms of their spin-density matrices. Since the absorptive single-pion-exchange model in question predicts identical values of the density matrix elements for both the $T_z = -\frac{3}{2}$ and $T_z = +\frac{1}{2}$ isobars, all the isobar events were combined in order to evaluate them experimentally. The density matrix elements ρ_{ij} were determined in terms of the moments of the experimentally observed angular distributions as follows:

$$\begin{aligned} \langle \cos^2\theta \rangle &= (1/15)(7 - 8\rho_{33}), \\ \langle \sin^2\theta \cos 2\phi \rangle &= (-8/5\sqrt{3}) \text{Re}\rho_{3-1}, \\ \langle \sin 2\theta \cos\phi \rangle &= (-8/5\sqrt{3}) \text{Re}\rho_{31}. \end{aligned} \quad (3)$$

In Eqs. (3) the left-hand sides are the experimentally determined moments of the given angular functions. In terms of experimental quantities, any one of them,

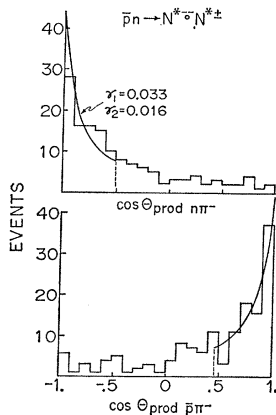


FIG. 3. Production angular distribution of the $T_z = -\frac{3}{2}$ isobars in the reactions $\bar{p}n \rightarrow \bar{N}^* N^*$ or $\bar{N}^* N^*$. The smooth curves are predictions of the absorptive single-pion-exchange model.

⁹ J. D. Jackson, Rev. Mod. Phys. **37**, 484 (1965); J. D. Jackson, J. T. Donohue, K. Gottfried, R. Keyser, and B. E. Y. Svensson, Phys. Rev. **139**, B428 (1965).

TABLE II. Spin-density matrix elements as calculated by the method of moments and least-squares fit for the combined resonances of the reaction $\bar{p}n \rightarrow \bar{N}^{*-}N^{*+}$ or $N^{*0}N^{*-}$.

Production cosine	Matrix element	Moment analysis	Least squares
≥ 0.8	ρ_{33}	0.221 ± 0.039	0.205 ± 0.045
≥ 0.8	ρ_{31}	0.017 ± 0.040	
≥ 0.8	ρ_{3-1}	-0.023 ± 0.038	-0.047 ± 0.026
0.5-0.8	ρ_{33}	0.187 ± 0.053	
0.5-0.8	ρ_{31}	-0.140 ± 0.050	
0.5-0.8	ρ_{3-1}	-0.049 ± 0.045	
< 0.5	ρ_{33}	0.226 ± 0.038	
< 0.5	ρ_{31}	0.070 ± 0.038	
< 0.5	ρ_{3-1}	-0.036 ± 0.039	

say $\langle f(\theta, \phi) \rangle$, is given by

$$\langle f(\theta, \phi) \rangle = \frac{1}{n} \sum_{i=1}^n f_i(\theta, \phi), \quad (4)$$

with an error

$$\delta \langle f \rangle = [(1/n) \langle f^2 \rangle - \langle f \rangle^2]^{1/2}. \quad (5)$$

In these equations, n is the total number of events used and $f_i(\theta, \phi)$ is the value of $f(\theta, \phi)$ for the i th event. The angles θ and ϕ are the usual decay angles defined in the isobar rest frame with respect to the incoming beam as quantization axis. Thus θ is the virtual scattering angle and ϕ is the Treiman-Yang angle. The matrix elements ρ_{33} and $\text{Re}\rho_{3-1}$ can also be determined by least-

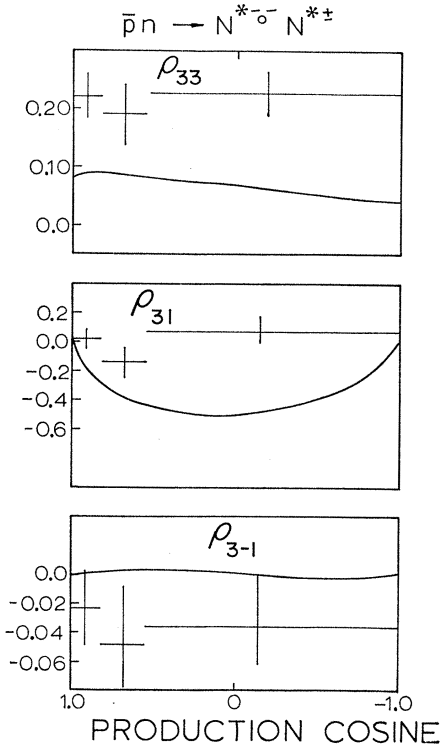


FIG. 4. Spin-density matrix elements of isobars produced in the reaction $\bar{p}n \rightarrow \bar{N}^{*0-}N^{*+}$. The smooth curves are the predictions of the absorptive single-pion-exchange model.

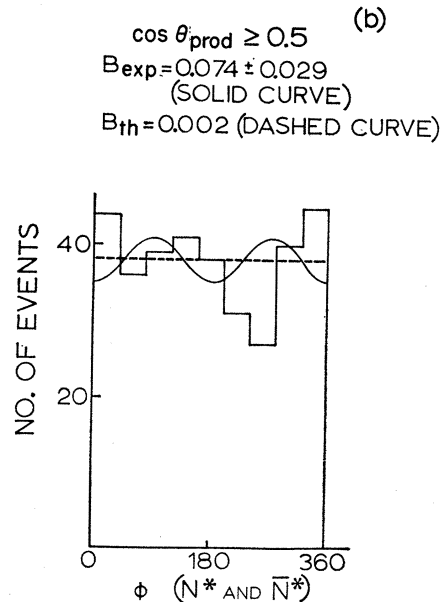
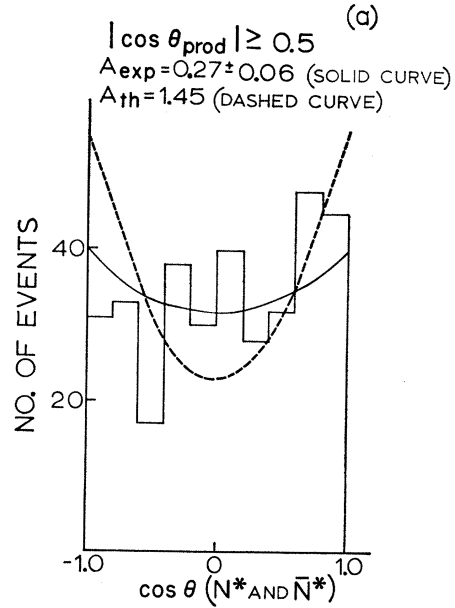
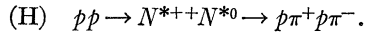


FIG. 5. Decay distributions of isobars in the reaction $\bar{p}n \rightarrow \bar{N}^{*0-}N^{*+}$. The solid curves are fits to the data of the form $1+A \cos^2\theta$ and $1+B \cos^2\phi$. The dashed curves are the predictions of the absorptive single-pion-exchange model.

squares fits to the experimental $\cos\theta$ and ϕ distributions, respectively. The results of the aforementioned calculations are displayed in Table II, in which are listed the experimentally determined density matrix elements for various cuts on the production angular distribution of the isobars. These results are compared with the predictions of the absorptive single-pion-exchange model in Fig. 4. In no case is there good agreement. The decay

angular distributions for the combined sample of double-resonance events are shown in Fig. 5. Only events for which $|\cos\theta_{\text{prod}}| \geq 0.5$ are included, thus removing any nonperipheral background. The solid curves shown on the figures are of the form $W(\theta) \sim 1 + A \cos^2\theta$ and $W(\phi) \sim 1 + B \cos^2\phi$. The coefficients depend on the density matrix elements and were evaluated by using the experimental density matrix elements appropriate to this range of $\cos\theta_{\text{prod}}$, as determined by the method of moments. The dashed curves were obtained by using the theoretical values of the density matrix elements over this range of $\cos\theta_{\text{prod}}$ to construct similar functions. The distribution in virtual scattering angle ($\cos\theta$) for the resonances (Fig. 5) shows a forward-backward asymmetry which persists for each isobar separately, and which is in disagreement with the predictions of the absorptive single-pion-exchange model. Thus, the predictions of the model are inconsistent with the observed features of double-isobar production in the reaction $\bar{p}n \rightarrow \bar{p}n\pi^+\pi^-$.

The quasi-two-body reactions (F) and (G) have as a counterpart in pp collisions the reaction



Reaction (H) is similar to reactions (F) and (G) in isotopic-spin structure in that it differs only in the sign of the third component, and thus (H) may be directly compared with (F) and (G). A similar comparison between the reactions $\bar{p}n \rightarrow \bar{N}^{*-}p \rightarrow \bar{p}\pi^-p$ and $pp \rightarrow N^{*++}n \rightarrow p\pi^+n$ was made by the Vanderbilt group.² One purpose of that comparison was to compare the experimental results with the predictions of the absorptive single-pion-exchange model. In Ref. 2 it was demonstrated that anti-isobar production occurred

somewhat more peripherally than isobar production, a result which was to be expected on the basis of the absorptive model predictions. This was so because the annihilation channels available in the $\bar{p}n$ reaction but not in the pp reaction would result in greater absorption of low partial waves in the former. A comparison of the double-isobar channels (F) and (G) with (H) constitutes a more stringent test of the absorptive one-pion-exchange model, since the predicted differences in production differential cross sections are detectably larger for these reactions than for the single-isobar production reactions.¹⁰

The analysis of the pp reaction is based on 1558 events of the type $pp \rightarrow pp\pi^+\pi^-$ taken from the earlier work of Pickup, Robinson, and Salant¹¹ and presented here in a form suitable for comparison with the $\bar{p}n$ interaction. Figure 6 shows the effective mass distribution for the $T_z = \frac{3}{2}$ and $T_z = \frac{1}{2}$ proton-pion combinations. Each histogram contains two contributions per event. The solid curves represent the predictions of Lorentz-invariant phase space. The presence of the $N^*(1238)$ is evident, although the signal in the $T_z = \frac{1}{2}$ plot is very weak. However, the background introduced by the incorrect $p\pi$ combinations is partly responsible for this. For comparison with the $\bar{p}n$ reaction and with the model, double-resonance events were chosen as described previously, namely, $1160 \leq (m_{p_1\pi} \text{ and } m_{p_2\pi}) \leq 1300$ MeV. This yielded 726 double-resonance events plus 73 events in which all four $p\pi$ masses fell within that mass range. The ambiguity was resolved, as in the $\bar{p}n$ reaction, by choosing the pair with the smallest value of squared four-momentum transfer.

The production angular distribution for these double-resonance events is shown in Fig. 7(a). Since the initial

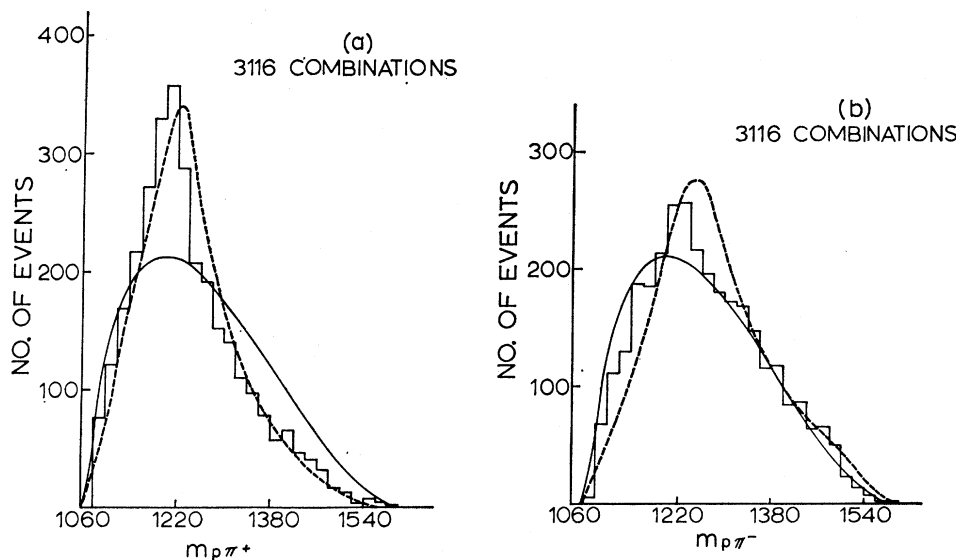


FIG. 6. (a) $m_{p\pi^+}$ and (b) $m_{p\pi^-}$ for 1558 events of the type $pp \rightarrow pp\pi^+\pi^-$. The solid curves represent Lorentz-invariant phase space. The dashed curves are the predictions of the absorptive single-pion-exchange model.

¹⁰ G. H. Hite and J. D. Jackson, University of Illinois, Urbana, Ill. (private communication).

¹¹ E. R. Pickup, D. K. Robinson, and E. O. Salant, Phys. Rev. 125, 2091 (1962).

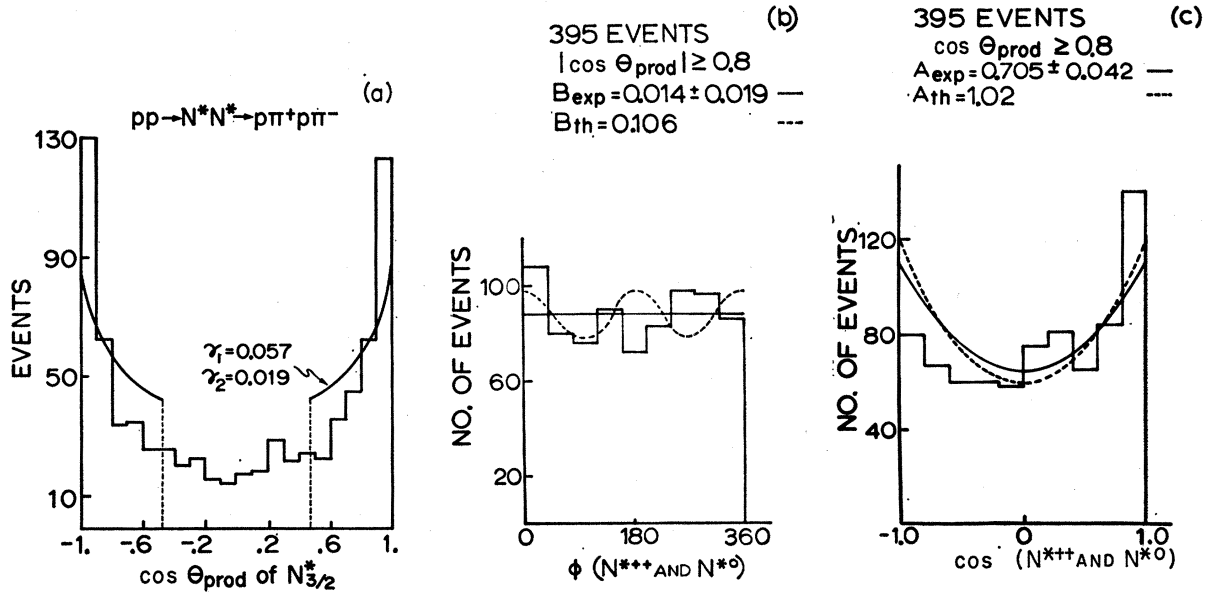


FIG. 7. (a) Production angular distribution of $N^*_{3/2}$ in the reaction $pp \rightarrow N^{*++}N^{*0}$. The smooth curve is the prediction of the absorptive single-pion-exchange model. (b) and (c) Decay distributions of the combined N^{*++} and N^{*0} events. The solid curves are fits to the data of the form $1+A \cos^2\theta$ and $1+B \cos^2\phi$. The dashed curves are the predictions of the absorptive single-pion-exchange model.

state contains identical protons, isobars should be produced with equal probability in the forward and backward directions in the pp center-of-mass frame. Thus, the distribution in $\cos\theta_{\text{prod}}$ should be symmetric about $\cos\theta_{\text{prod}}=0$. The solid curve is the prediction of the absorptive single-pion-exchange model⁹ normalized to the number of events in the region $|\cos\theta_{\text{prod}}| \geq 0.5$. As with the $\bar{p}n$ reaction, the absorptive parameters γ_1 and γ_2 were those which gave best agreement with the data for the corresponding single-isobar reaction. The measured cross section over this range of production angle was 0.9 mb, while the model predicted 2.6 mb.

There is noticeable disagreement between the histogram and the solid curve of Fig. 7(a). The isobars are produced much more peripherally than the model predicts and, in fact, more peripherally than those of the $\bar{p}n$ reaction. Omission of the 73 ambiguous events from the sample produced no significant difference in

the results. Thus, double-isobar production in the pp reaction is more peripheral than double-isobar production in the $\bar{p}n$ reaction, contrary to the predictions of the absorptive single-pion-exchange model.

TABLE III. Spin-density matrix elements as calculated by the method of moments and least-squares fit for the combined resonances of the reaction $pp \rightarrow N^{*++}N^{*0}$.

Production cosine	Matrix element	Moment analysis	Least squares
≥ 0.8	ρ_{33}	0.155 ± 0.022	0.139 ± 0.038
≥ 0.8	ρ_{31}	-0.054 ± 0.020	
≥ 0.8	ρ_{3-1}	0.006 ± 0.019	0.001 ± 0.029
0.5-0.8	ρ_{33}	0.193 ± 0.029	0.200 ± 0.015
0.5-0.8	ρ_{31}	-0.017 ± 0.029	
0.5-0.8	ρ_{3-1}	0.010 ± 0.028	-0.015 ± 0.039
< 0.5	ρ_{33}	0.216 ± 0.027	0.217 ± 0.027
< 0.5	ρ_{31}	0.028 ± 0.029	
< 0.5	ρ_{3-1}	-0.024 ± 0.028	-0.011 ± 0.042

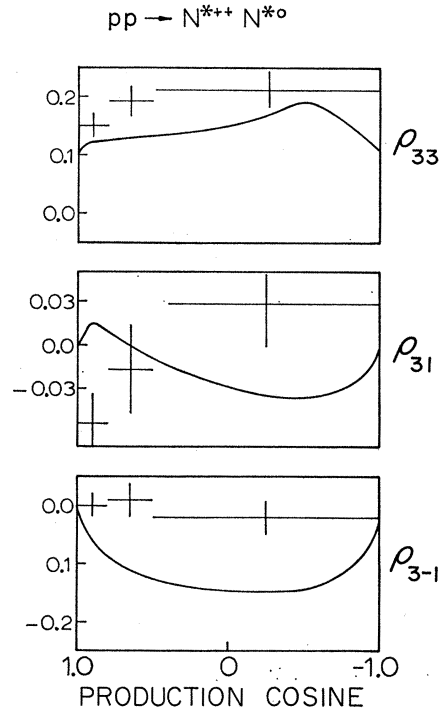


FIG. 8. Spin-density matrix elements of the combined isobars in the reaction $pp \rightarrow N^{*++}N^{*0}$. The smooth curves are the predictions of the absorptive single-pion-exchange model.

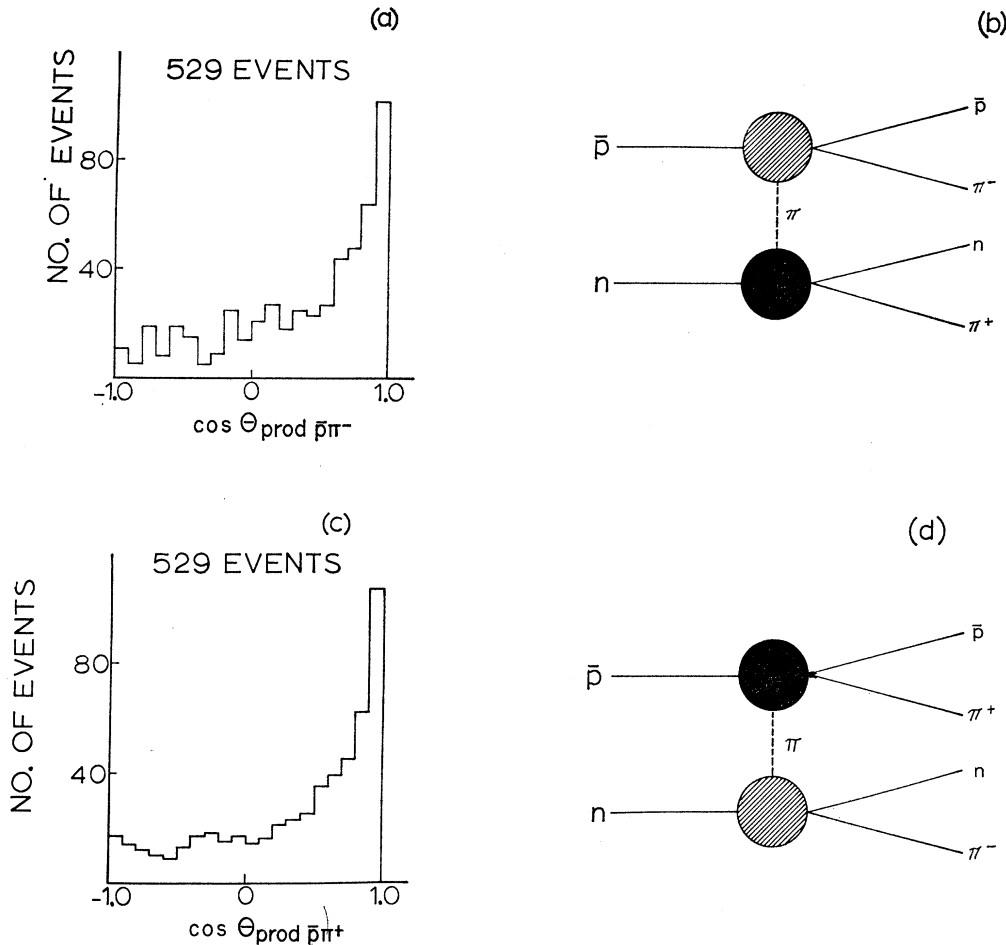


FIG. 9. (a) and (b) Production angular distribution and single-pion-exchange diagram for the $\bar{p}\pi^-$ system in the reaction $\bar{p}n \rightarrow \bar{p}n\pi^+\pi^-$. (c) and (d) Same for the $n\pi^+$ system in this reaction.

The decay angular distributions of the isobars are shown in Figs. 7(a) and 7(b). Only events for which $|\cos\theta_{\text{prod}}| \geq 0.8$ are shown; and, as with the $\bar{p}n$ analysis, the N^{*++} and N^{*0} distributions are combined. The angles θ and ϕ are identical with those discussed above in connection with the $\bar{p}n$ reaction. The solid curves in Figs. 7(b) and 7(c) were obtained by using the experimentally determined spin-density matrix elements to construct functions of the form $W(\theta) \sim 1 + A \cos^2\theta$ and $W'(\phi) \sim 1 + B \cos^2\phi$. The dashed curves were obtained in a similar fashion, but with the theoretical values of the spin-density matrix elements. In this case, the agreement between the dashed and solid curves of Fig. 7(c) is quite good, unlike the $\bar{p}n$ reaction [Fig. 5(a)]. However, this agreement means little, since the theoretical distribution in $\cos\theta$ depends on the density matrix element ρ_{33} , which in turn depends only on the average value of $\cos^2\theta$ for all the events. This average clearly does not reflect the large asymmetry in the experimental $\cos\theta$ distribution. The experimental density matrix elements are listed in Table III and

compared with the absorptive model predictions in Fig. 8. Once again the agreement is, in general, not good.

The above results indicate that the absorptive single-pion-exchange model does not explain the dynamics of the reaction $\bar{p}p \rightarrow N^{*++}N^{*0} \rightarrow \bar{p}p\pi^+\pi^-$. Most important perhaps is the fact that while this model predicts that the reactions $\bar{p}n \rightarrow \bar{N}^{*-}N^{*+}$ and $\bar{p}n \rightarrow \bar{N}^{*0}N^{*-}$ should occur more peripherally than the reaction $\bar{p}p \rightarrow N^{*++}N^{*0}$, just the opposite is true experimentally. This is in sharp contrast to our previous results² concerning single-isobar and anti-isobar production in the reactions $\bar{p}n \rightarrow \bar{N}^{*-}p$ and $\bar{p}p \rightarrow N^{*++}n$.

The most obvious problem in analyzing the data in terms of the absorptive calculations described above is that the calculations make no allowance for possible nonresonant contributions to the reactions. In an earlier paper concerning the reaction $\bar{p}p \rightarrow \bar{p}p\pi^+\pi^-$, a slightly more general single-pion-exchange model was formulated¹¹ which allows for this possibility. This model was also applied to the reactions under consideration here. It can be explained with the help of Figs. 9(b) and 9(d).

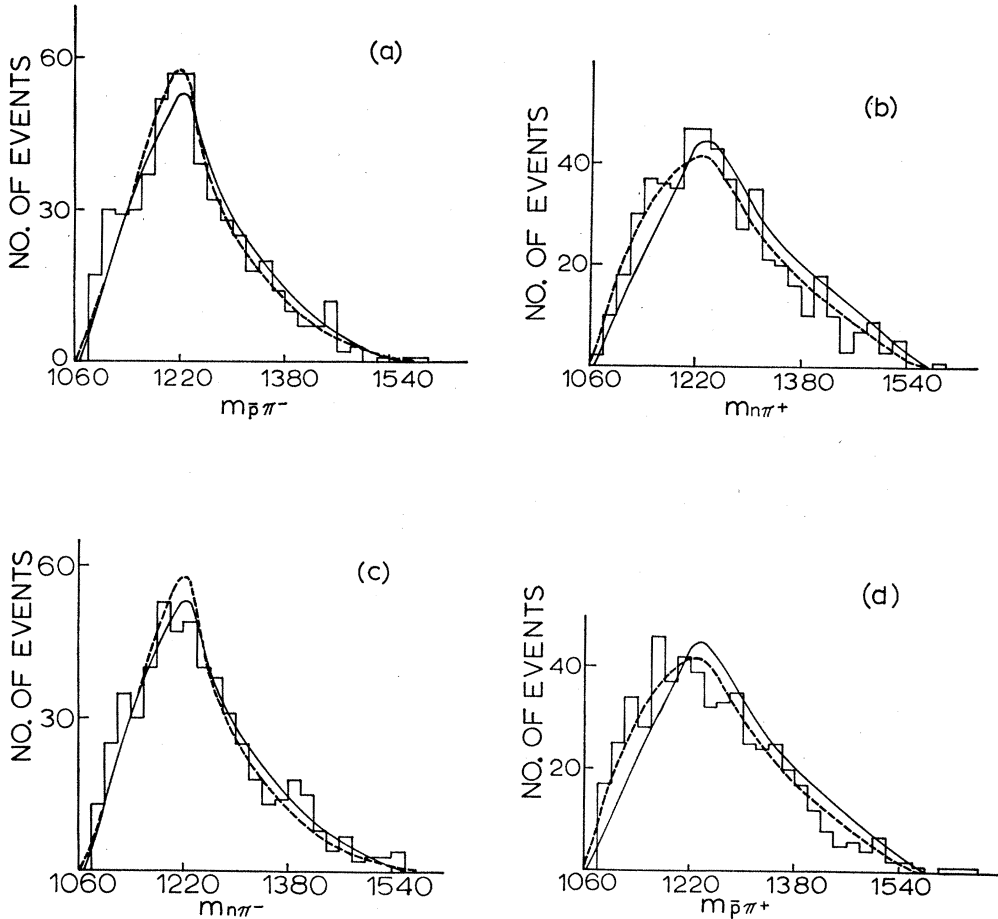


FIG. 10. Effective masses of (a) $\bar{p}\pi^-$, (b) $n\pi^+$, (c) $n\pi^-$, and (d) $\bar{p}\pi^+$ systems in the reaction $\bar{p}n \rightarrow \bar{p}n\pi^+\pi^-$. The solid curves are the predictions of the double-scattering model plus phase space. The dashed curves are the predictions of this model plus $N^*(1400)$ and $N^*(1400)$ production as described in the text.

In these figures, possible Feynman diagrams for the reactions (F) and (G) are shown schematically. The contribution to the cross section from either of these diagrams has the general form

$$d\sigma \sim |V_I|^2 F(t) |V_{II}|^2. \quad (6)$$

In Eq. (6), V_I and V_{II} are vertex functions which are associated with the shaded circles in the figure. The function $F(t)$ contains the propagator for the exchanged pion and any form factors connected with vertex and propagator corrections. The variable t is the square of the four-momentum transfer from the incoming \bar{p} to the outgoing $\bar{p}\pi^-$ or $\bar{p}\pi^+$ system.

The feature of the more general single-pion-exchange model, which distinguished it from the absorptive model discussed above, was the choice of the vertex functions V_I and V_{II} . In the absorptive single-pion-exchange model, these vertex functions described the coupling of the incoming baryon or antibaryon to the outgoing $T=\frac{3}{2}$ isobar and the virtual exchanged pion. In the more general model, hereafter called the double-

scattering model, the vertex functions were constructed so as to describe the elastic scattering of the virtual pion by the incoming baryon or antibaryon. Moreover, the off-shell elastic scattering was assumed to be well approximated by on-the-mass-shell pion-nucleon scattering. Quantitatively, then, either V_I or V_{II} was expressed as

$$|V|^2 = (8\pi\omega)^2 d\sigma(\omega, \cos\theta)/d\Omega. \quad (7)$$

In (7), V is either V_I or V_{II} , ω is the effective mass of the nucleon-(antinucleon-) pion system of the vertex in question, $\cos\theta$ is the virtual scattering angle of the outgoing baryon with respect to the incoming baryon in the ω rest frame, and $d\sigma(\omega, \cos\theta)/d\Omega$ is the appropriate on-the-mass-shell pion-nucleon differential scattering cross section. It is clear that in each of the diagrams of Fig. 9, one vertex corresponds to pure $T=\frac{3}{2}$ elastic pion-nucleon scattering, while the other is a combination of $T=\frac{1}{2}$ and $T=\frac{3}{2}$ elastic scattering. For the actual calculations, $d\sigma(\omega, \cos\theta)/d\Omega$ was in each case obtained

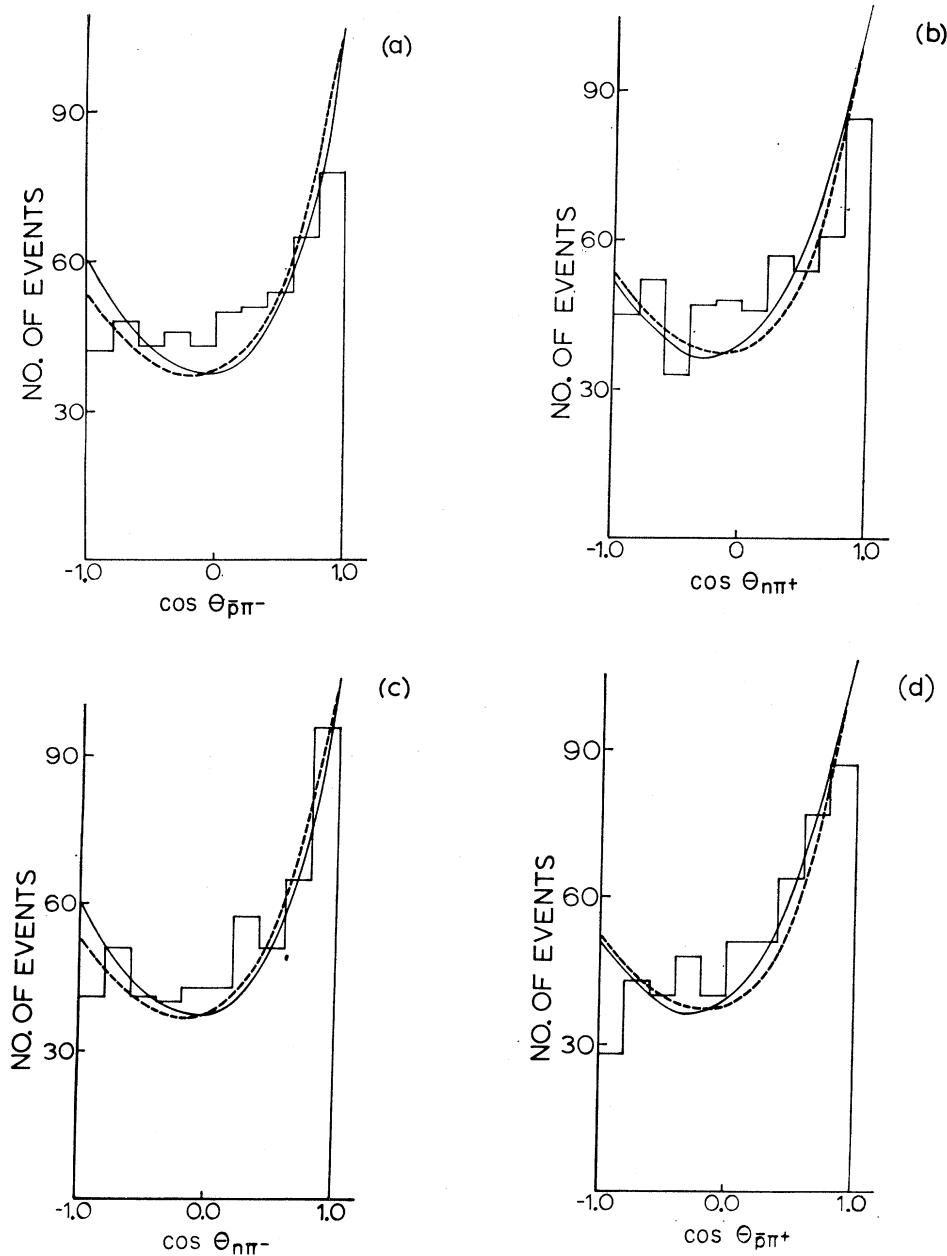


FIG. 11. Scattering angular distributions in the rest frame of (a) $p\pi^-$, (b) $n\pi^+$, (c) $n\pi^-$, and (d) $\bar{p}\pi^+$ systems in the reaction $\bar{p}n \rightarrow \bar{p}n\pi^+\pi^-$. The solid and dashed curves are in one-to-one correspondence with those described in Fig. 10.

from experimental pion-nucleon scattering data¹² over the range of energies contained within our phase-space limits. Thus the theoretical mass distribution corresponding to the pure $T=\frac{3}{2}$ vertex reflects the strong production of the $N^*(1238)$ isobar, and the distribution corresponding to the opposite vertex reflects production of both the $N^*(1238)$ and $N^*(1520)$ isobars.

¹² D. C. Wood, T. J. Devlin, J. A. Helland, M. J. Longo, B. J. Moyer, and V. Perez-Mendez, *Phys. Rev. Letters* **6**, 481 (1961); J. A. Helland, T. J. Devlin, D. E. Hagge, M. J. Longo, and B. J. Moyer, *Phys. Rev.* **134**, B1079 (1964); P. M. Ogden *et al.*, *ibid.* **137**, B1115 (1965); J. A. Helland *et al.*, *ibid.* **134**, B1062 (1964). See also G. Källén, *Elementary Particle Physics* (Addison-Wesley, Reading, Mass., 1964), p. 72.

The function $F(t)$ was in each case chosen in such a way as to match the appropriate experimental distribution. As already pointed out in connection with Fig. 3, the absorptive single-pion-exchange model could be parametrized so as to give good agreement with the experimental production angular distributions for double-isobar events and, in fact, also with the t distributions for those events, since the latter distributions are strongly dependent on the former. Moreover, it was found that these absorptive model predictions characterized the experimental t distributions for all (not just double-isobar) events fairly well. Thus, the form of $F(t)$ in each case was taken directly from the absorp-

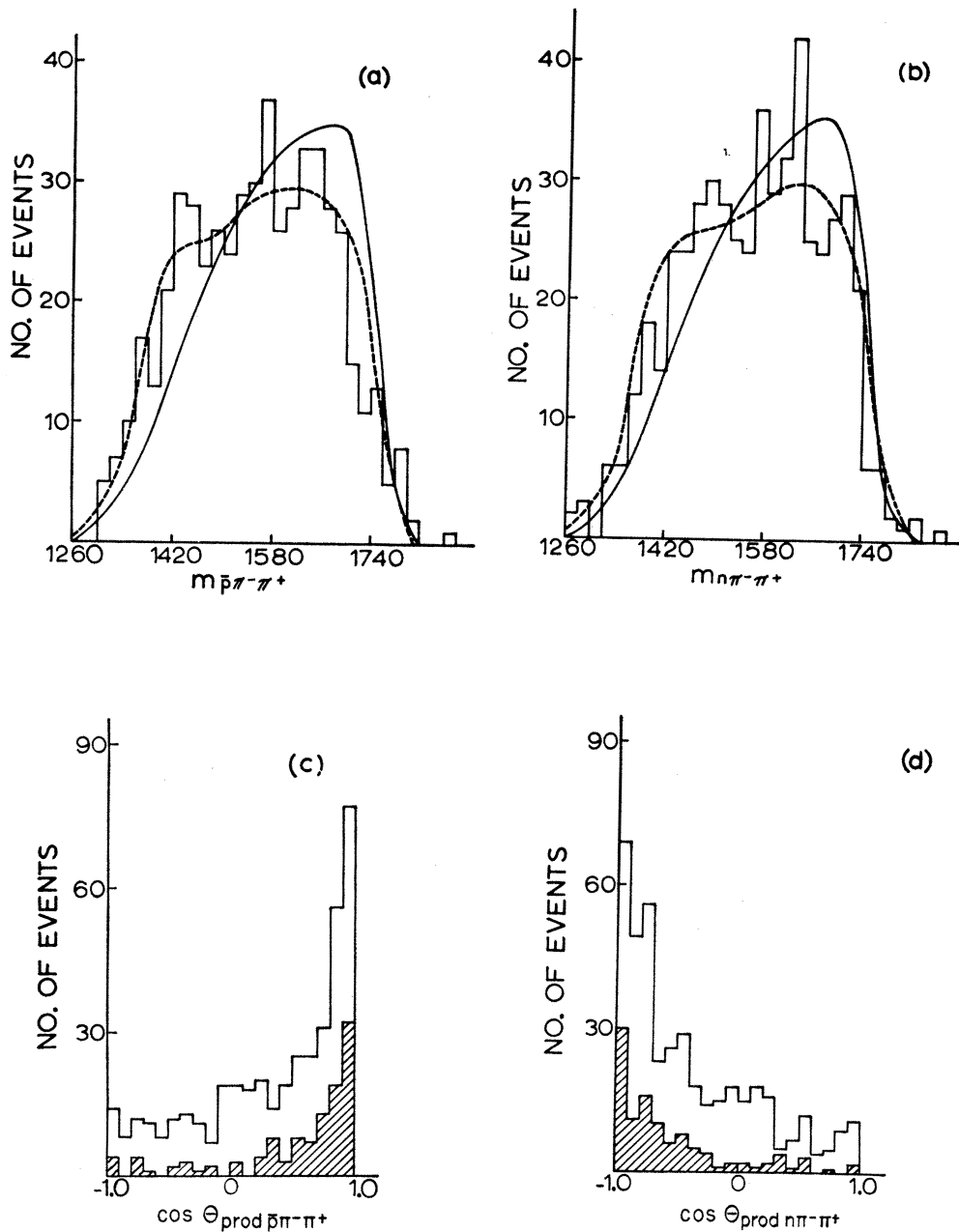


FIG. 12. (a) $M_{\bar{p}\pi^+\pi^-}$ and (b) $M_{n\pi^+\pi^-}$ mass spectra in the reaction $\bar{p}n \rightarrow \bar{p}n\pi^+\pi^-$. The solid and dashed curves again are in correspondence with those described in Figs. 10(c) and 10(d). Production angular distributions of the $\bar{p}\pi^+\pi^-$ and $n\pi^+\pi^-$ systems outside and inside (shaded events) the 1400-MeV mass region.

tive single-pion-exchange model. In other words, the differential cross sections $d\sigma/d \cos\theta_{\text{prod}}$ predicted by the double-scattering model were essentially the solid curves of Fig. 3. Finally, the absence of any dependence of the vertex functions on the azimuthal angle ϕ is in accord with the observed consistency of the Treiman-Yang distributions [Fig. 5(b)] with isotropy.

A theoretical model was constructed which consisted of three contributions to the cross section for the reaction $\bar{p}n \rightarrow \bar{p}n\pi^+\pi^-$. Two of these contributions arose from the two single-pion-exchange diagrams of Fig. 9, as discussed in the preceding paragraph, and the third

was Lorentz-invariant phase space. These contributions were added incoherently, and the fraction of each in the sum was determined by making least-squares fits to the experimental nucleon- (antinucleon-) pion mass and angular distributions. The best over-all fit to all the data was obtained when each of the single-pion-exchange diagrams contributed $(40 \pm 7)\%$, while the phase-space contribution was $(20 \pm 5)\%$. Again, this result was a useful check on the data analysis and on the model because each of the single-pion-exchange diagrams should contribute equally to the cross section for the whole reaction.

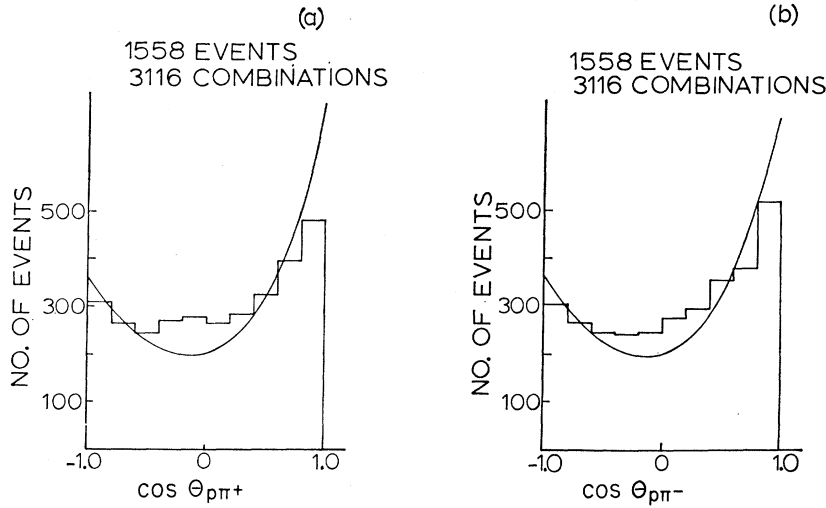
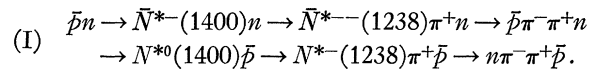


FIG. 13. Scattering angular distributions in the rest frame of (a) the $p\pi^+$ and (b) the $p\pi^-$ systems in the reaction $p\bar{p} \rightarrow p\bar{p}\pi^+\pi^-$. The solid curves are the predictions of the double-scattering model.

In Fig. 10 all experimental nucleon- (antinucleon-) pion mass distributions are shown again. The solid curves are the predictions of the theoretical model that best fits the data, namely, that model in which each single-pion-exchange diagram contributes 40%. The agreement in all cases is satisfactory. In Fig. 11 the virtual scattering angular distributions are shown for all nucleon- (antinucleon-) pion systems. Note that if the four histograms of Fig. 11 are added together, and if the double-isobar and production angle cuts are imposed, the cosine distribution previously discussed in Fig. 5 is obtained. It is particularly important to note that the double-scattering model includes isobar and nonisobar contributions to the reaction, and hence neither of these cuts is necessary. The forward-backward asymmetry mentioned in connection with Fig. 5 is evident in all the distributions of Fig. 11. Noteworthy, however, is the fact that the solid curves which represent the predictions of the double-scattering model plus phase space also show a marked forward-backward asymmetry. While the agreement between the experimental angular distributions and the solid curves is not spectacular, it is clear that these curves are much better fits to the data than either the solid or dashed curves of Fig. 5, which are the predictions of the absorptive single-pion-exchange model. Thus it is concluded that the predictions of the double-scattering model are in better agreement with the observed two-body mass and angular distributions than are the predictions of the absorptive single-pion-exchange model.

As a further check on the validity of this model, the mass distributions of the $\bar{p}\pi^-\pi^+$ and $n\pi^-\pi^+$ systems were studied. These are shown in Figs. 12(a) and (12b). Again, the solid curves are the predictions of the double-scattering model plus phase space. The agreement here is less satisfactory than for the two-body distributions. In particular, the data show a tendency to peak above the model in the low-mass region near 1400 MeV. (A similar peaking in the $\bar{p}\pi^-\pi^+$ and $p\pi^-\pi^+$ mass spectra

from the companion reaction $\bar{p}p \rightarrow \bar{p}p\pi^+\pi^-$ at this energy has been discussed in a previous paper¹ and will be dealt with more fully in a separate communication.) An attempt was made to improve the agreement between the data and the theoretical model by adding to the model two more amplitudes which describe the production of $\bar{N}^*(1400)$ and $N^*(1400)$ states. These were assumed to decay sequentially as follows:



The decays are all assumed to be isotropic in the rest frame of the decaying particle, with the incoming beam chosen as the quantization axis. This assumption was made for the sake of simplicity, but would in fact be the correct one if the spin of the 1400-MeV state were $\frac{1}{2}$. The amplitudes describing the production of these states were added incoherently as fourth and fifth contributions to the model discussed in the preceding paragraph.

Again, least-squares fits to the data were made to determine the best values of mass and width of the 1400-MeV states and also to determine the fraction of each of the individual contributions to the entire reaction. The best fit to all the data was obtained when the mass of the $N^*(1400)$ systems was 1.410 ± 0.010 GeV and the width 0.080 ± 0.020 GeV. Moreover, this fit required that the previously discussed double-scattering diagrams of Figs. 9(b) and 9(d) each contribute 30% while each of the $N^*(1400)$ amplitudes contribute 20%. No phase space was required by this fit. The error bars in all cases were 7–10%. The predictions of the model so amended are shown by the dashed curves in Figs. 10–12. As far as the two-body mass and angular distributions are concerned (Figs. 10 and 11), the replacement of the phase-space contribution by the $N^*(1400)$ production amplitudes caused only small changes in the predictions of the model, and,

if anything, the differences were such as to improve the fits to the two-body mass distributions. The fits to the three-body mass distributions were also improved, as can be seen by comparing the solid and dashed curves in Figs. 12(a) and 12(b). This is not surprising, since the aim in adding the $N^*(1400)$ amplitudes was precisely to obtain better agreement with the experimental three-body mass distributions. It is important to note, moreover, that the addition of these amplitudes accomplishes this purpose without destroying the agreement between the experimental and theoretical two-body mass and angular distributions. This is entirely similar to the situation encountered in Ref. 1 in a study of the reaction $\bar{p}p \rightarrow \bar{p}p\pi^+\pi^-$.

In Figs. 12(c) and 12(d) are shown the experimental distributions in $\cos\theta_{\text{prod}}$ for the three-body systems in the center-of-mass frame of the incoming antiproton and target neutron. In both cases the angle has been measured relative to the antiproton. The shaded events are those which have the appropriate three-body mass inside the $N^*(1400)$ mass region, defined as $1380 \leq m_{N\pi\pi} \leq 1480$ MeV. The unshaded events are those for which this mass lies outside the $N^*(1400)$ region. There is a slight tendency for events inside the $N^*(1400)$ regions to be produced more peripherally than those outside, but this effect is not pronounced.

A fit of the form e^{-bt} was made to the t distributions of the $N^*(1400)$ events. Here t is the square of the four-momentum transfer from the incoming $\bar{p}(n)$ to the outgoing $\bar{p}\pi^-\pi^+(n\pi^-\pi^+)$ system. For this purpose, only events with $0.08 \leq t \leq 0.20$ $(\text{GeV}/c^2)^2$ were chosen in order to include peripherally produced events, but to avoid the kinematic constraint imposed by the lower boundary of the Chew-Low plot. The values of the slope obtained in this manner were

$$b_{\bar{N}^*} = 2.6 \pm 3.7 \text{ (GeV}/c^2\text{)}^{-2} \text{ for the } \bar{N}^*(1400),$$

$$b_{N^*} = 10.2 \pm 6.4 \text{ (GeV}/c^2\text{)}^{-2} \text{ for the } N^*(1400).$$

The large error bars reflect the statistically small sample of events remaining after all cuts were made.

In passing, we note that the mass, width, and slope of the t distribution for the enhancements observed in this experiment are not in agreement with the corres-

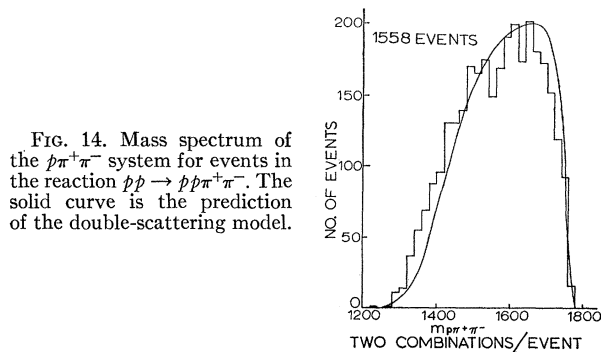


FIG. 14. Mass spectrum of the $p\pi^+\pi^-$ system for events in the reaction $pp \rightarrow pp\pi^+\pi^-$. The solid curve is the prediction of the double-scattering model.

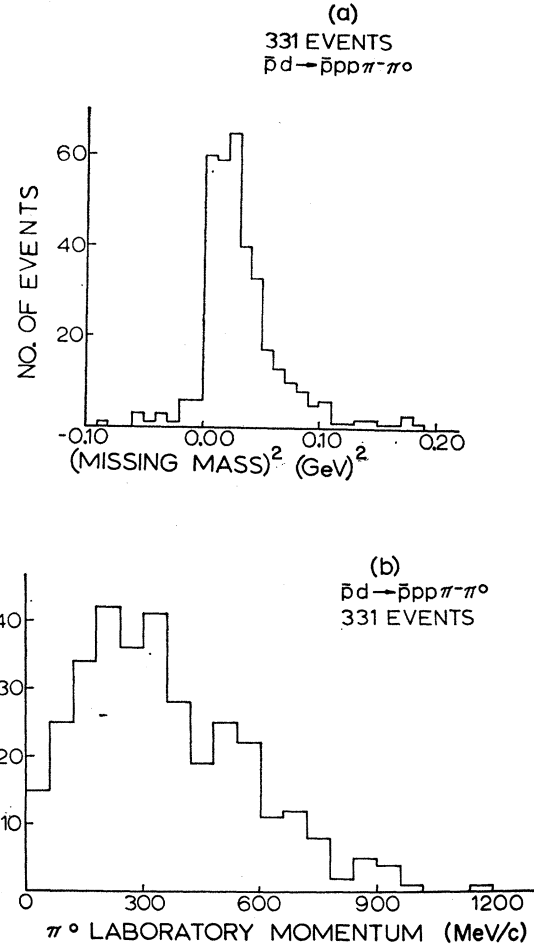


FIG. 15. (a) Missing mass squared for events satisfying the hypothesis $\bar{p}d \rightarrow \bar{p}pp\pi^-\pi^0$. (b) Fitted laboratory momentum of the π^0 .

ponding parameters for the $T = \frac{1}{2}$ $N^*(1470)$ Roper resonance.¹³

To complete the comparison of the $\bar{p}n$ reaction with the pp reaction, the double-scattering model was also applied to the latter. The calculations for the pp reaction were essentially the same as those for the $\bar{p}n$ reaction, although in this case it was necessary to in-

¹³ This resonance was originally discussed within the framework of a pion-nucleon phase-shift analysis by L. David Roper, Phys. Rev. Letters 12, 340 (1964). Since then, a number of counter groups have observed enhancements between 1400 and 1470 MeV in the missing-mass spectrum from the reaction $pp \rightarrow p +$ (missing mass). See, for example, G. Cocconi *et al.*, Phys. Letters 8, 134 (1964); C. M. Ankenbrandt *et al.*, Nuovo Cimento 35, 1052 (1965); G. Belletini *et al.*, Phys. Letters 18, 167 (1965); E. W. Anderson *et al.*, Phys. Rev. Letters 16, 855 (1966); I. M. Blair *et al.*, *ibid.* 17, 789 (1966); K. J. Foley *et al.*, *ibid.* 19, 397 (1967). Several bubble-chamber groups have also reported the observation of similar enhancements in the mass spectra of $T_z = \frac{1}{2}$ $N\pi$ and $N\pi\pi$ systems produced in pp , Kp , and πp collisions. See S. L. Adelman, *ibid.* 13, 555 (1964); E. Gellert *et al.*, *ibid.* 17, 884 (1966); S. P. Almeida *et al.*, Nuovo Cimento 50A, 1000 (1967); R. B. Bell *et al.*, Phys. Rev. Letters 20, 164 (1968); E. L. Berger *et al.*, *ibid.* 20, 964 (1968); W. E. Ellis *et al.*, *ibid.* 21, 697 (1968); R. A. Jespersen *et al.*, *ibid.* 21, 1368 (1968).

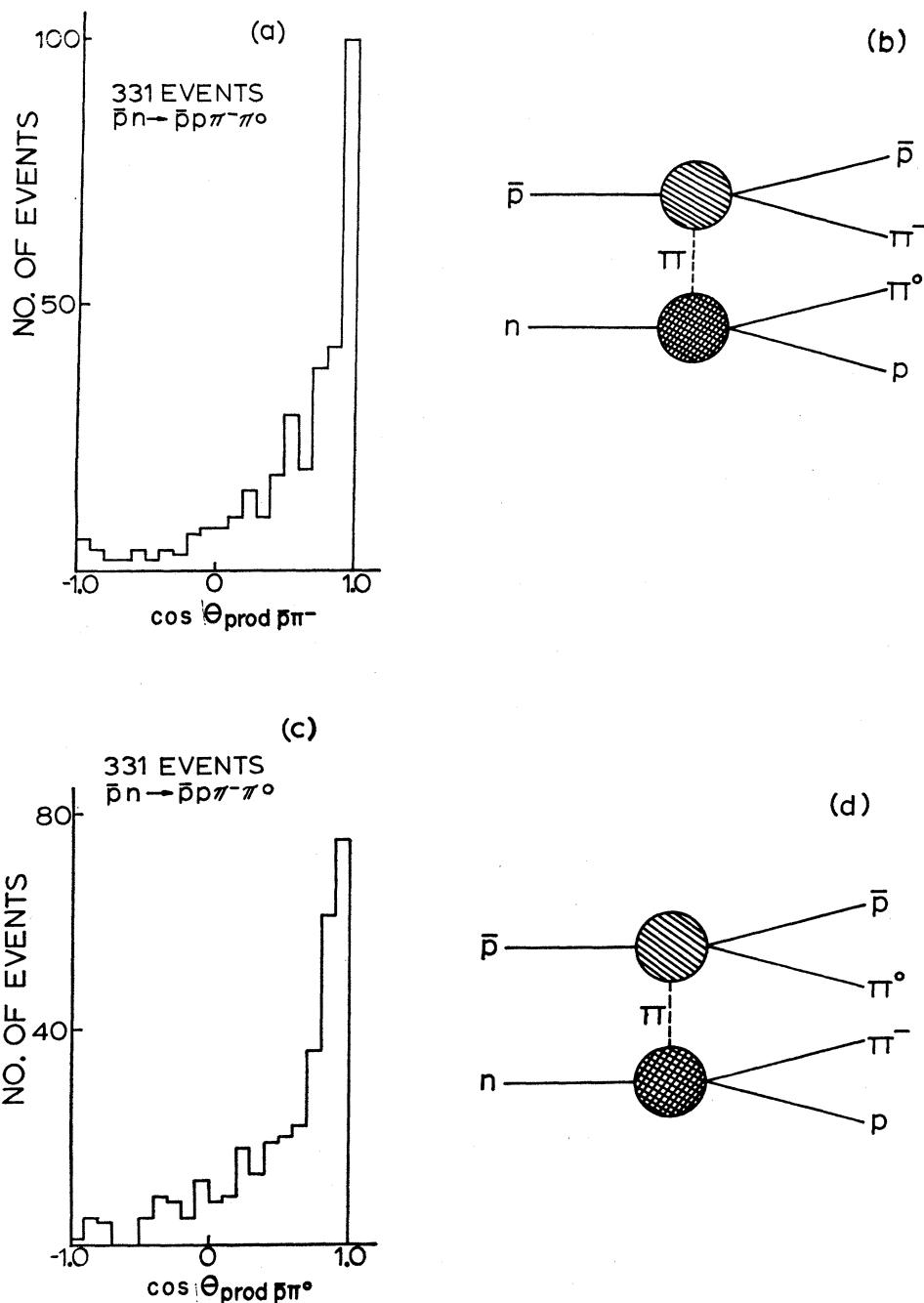


FIG. 16. (a) and (b) Production angular distributions and single-pion-exchange diagram for the $\bar{p}\pi^-$ system. (c) and (d) Same for the $\bar{p}\pi^0$ systems.

clude symmetrization effects due to the identity of the two protons. Also, the function $F(t)$ of Eq. (6) was in this case taken directly from the experimental data and thus automatically included the extremely peripheral production angular distribution of Fig. 7(a).

The dashed curves in Fig. 6, representing the $p\pi^+$ and $p\pi^-$ mass spectra predicted by the double-elastic-scattering model, are in fair agreement with the data. The scattering angular distributions are shown together with the predictions of the model (solid curves) in

Fig. 13. This figure is similar to Fig. 7(c) except that no mass or angle cuts were imposed. Once again, as with the $\bar{p}n$ reaction, the observed asymmetry in these distributions is matched by the predictions of the model.

Finally, Fig. 14 shows the $p\pi^+\pi^-$ mass spectrum. Here, each event was plotted twice and the solid curve is again the prediction of the double-scattering model. The agreement is fairly good, and, in particular, evidence for an enhancement in the 1400-MeV mass

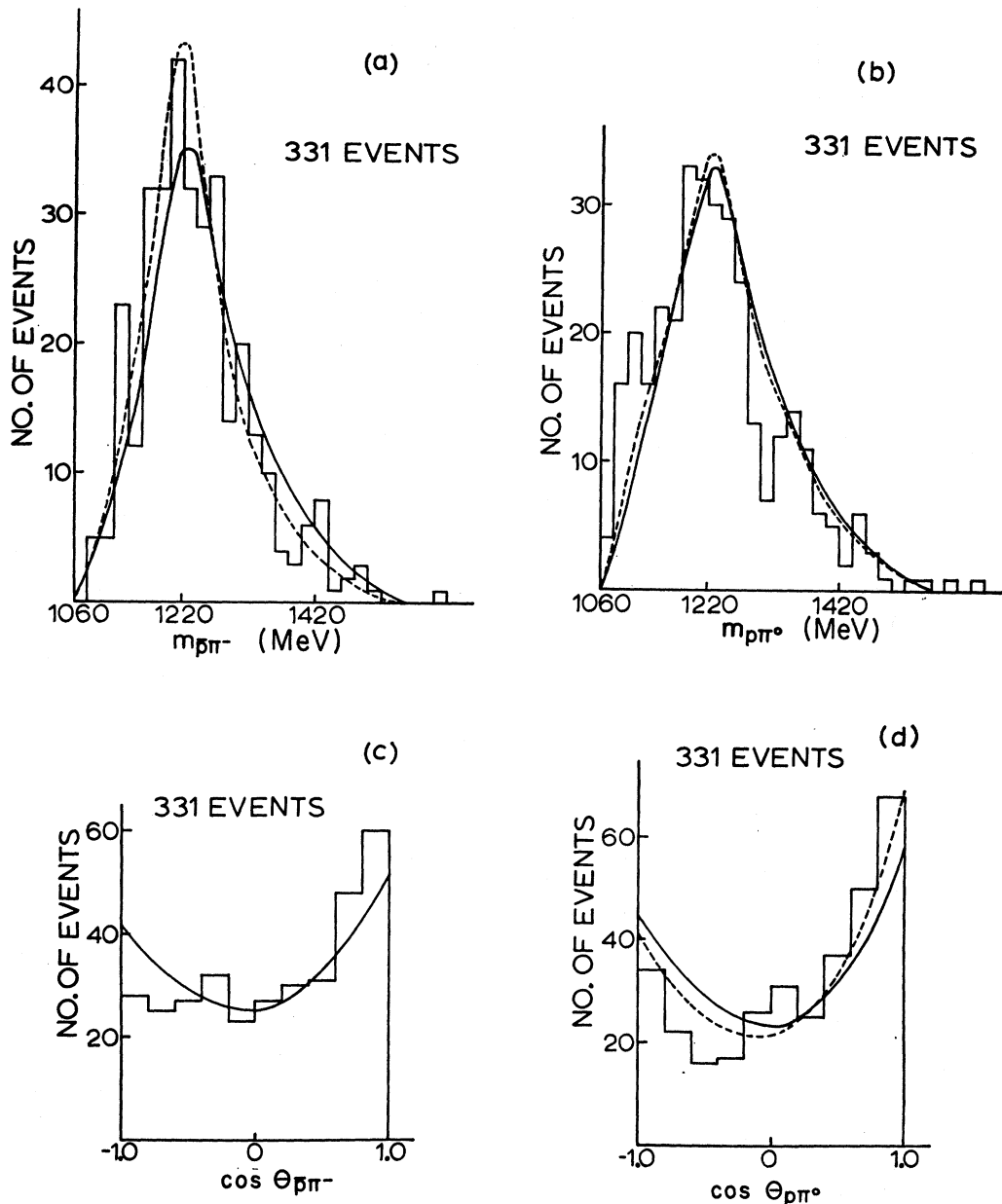


FIG. 17. (a) and (b) Effective mass distributions for the $\bar{p}\pi^-$ and $p\pi^0$ systems from the reaction $\bar{p}p \rightarrow \bar{p}p\pi^-\pi^0$. The solid curves are predictions of the double-scattering model plus phase space. The dashed curves are the predictions of the double-scattering model plus $\bar{N}^*(1400)$ production plus phase space, as described in the text. (c) and (d) Virtual scattering angular distributions of the \bar{p} and p in the $\bar{p}\pi^-$ and $p\pi^0$ rest frames. The curves are as described above.

region is very weak. Accordingly, no attempt to modify the model further was undertaken.

V. REACTION $\bar{p}n \rightarrow \bar{p}p\pi^-\pi^0$

The kinematic fitting programs successfully fitted 541 events to the hypothesis $\bar{p}d \rightarrow \bar{p}p\pi^-\pi^0(p)$ with spectator-proton momentum less than 250 MeV/c. However, 210 of these events also fitted the single-pion production hypothesis $\bar{p}d \rightarrow \bar{p}p\pi^-(p)$. Furthermore, the criteria outlined in Sec. I for assigning fits to various

categories were of no help in resolving these ambiguities, since all the criteria were obeyed by both the single- and double-pion fits. In an attempt to resolve this problem, the mass and angular distributions for these events were obtained by first assuming that they were all of type (E), namely, $\bar{p}d \rightarrow \bar{p}\pi^-p(p)$, and then assuming that they were all of type (B), $\bar{p}d \rightarrow \bar{p}p\pi^-\pi^0(p)$. The resulting distributions were then compared with the corresponding distributions from unambiguous fits of types (E) and (B), respectively.

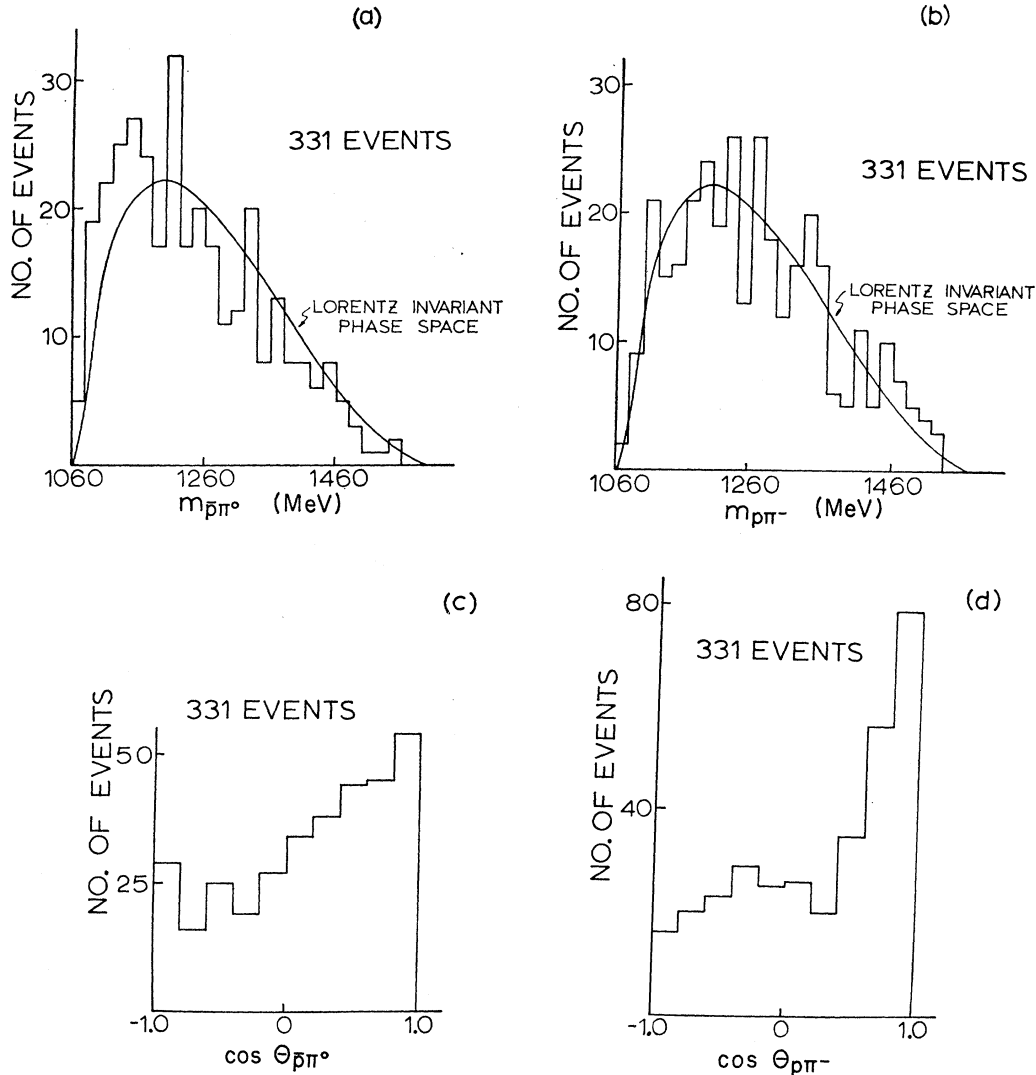


FIG. 18. Effective mass distributions of (a) the $\bar{p}\pi^0$ and (b) the $p\pi^-$ system in the reaction $\bar{p}n \rightarrow \bar{p}\pi^-\pi^0$. Virtual scattering angular distributions of (c) the \bar{p} and (d) the p in the $\bar{p}\pi^0$ and $p\pi^-$ rest frames, respectively.

It was found that the 210 ambiguous events behaved in all respects like the unambiguous single-pion production events. On the other hand, when considered as double-pion production events, there was considerable disagreement between the various distributions of the ambiguous events and those of the unambiguous double-pion fits. In particular, the $\bar{p}\pi^0$ and $p\pi^0$ effective mass plots for the ambiguous events peaked at 1150 MeV, with 95% of the events below 1220 MeV. Of the 210 ambiguous events, 170 had π^0 laboratory momentum less than 200 MeV/c. In addition, the azimuthal decay distributions of the $\bar{p}\pi^0$ and $p\pi^0$ systems in their respective rest frames were peaked near 0° , whereas for the unambiguous double-pion fits, these distributions were isotropic. On the other hand, the mass and angular distributions of the $\bar{p}\pi^-$ and $p\pi^-$ systems in both the ambiguous and unambiguous fits were very similar.

In view of these observations, it was concluded that the 210 ambiguous events were single-pion production events of type (E) to which a slow π^0 had been spuriously added. Thus, these events were not included in the subsequent analysis of channel (B), $\bar{p}n \rightarrow \bar{p}\pi^-\pi^0$. The remaining 331 events in this channel correspond to a cross section of 0.9 ± 0.1 mb. The square of the missing mass for these events and their fitted π^0 laboratory momentum distribution are shown in Fig. 15. It is to be noted that the squared missing-mass spectrum peaks near $(m_{\pi^0})^2$ and shows no particular structure otherwise.

The production angular distributions of $\bar{p}\pi^-$ and $\bar{p}\pi^0$ systems are displayed in Figs. 16(a) and 16(c). Here, θ_{prod} is the angle between the incident \bar{p} and the outgoing $\bar{p}\pi^-$ or $\bar{p}\pi^0$ system in the $\bar{p}n$ center-of-mass frame. Figures 16(b) and 16(d) show the Feynman diagrams

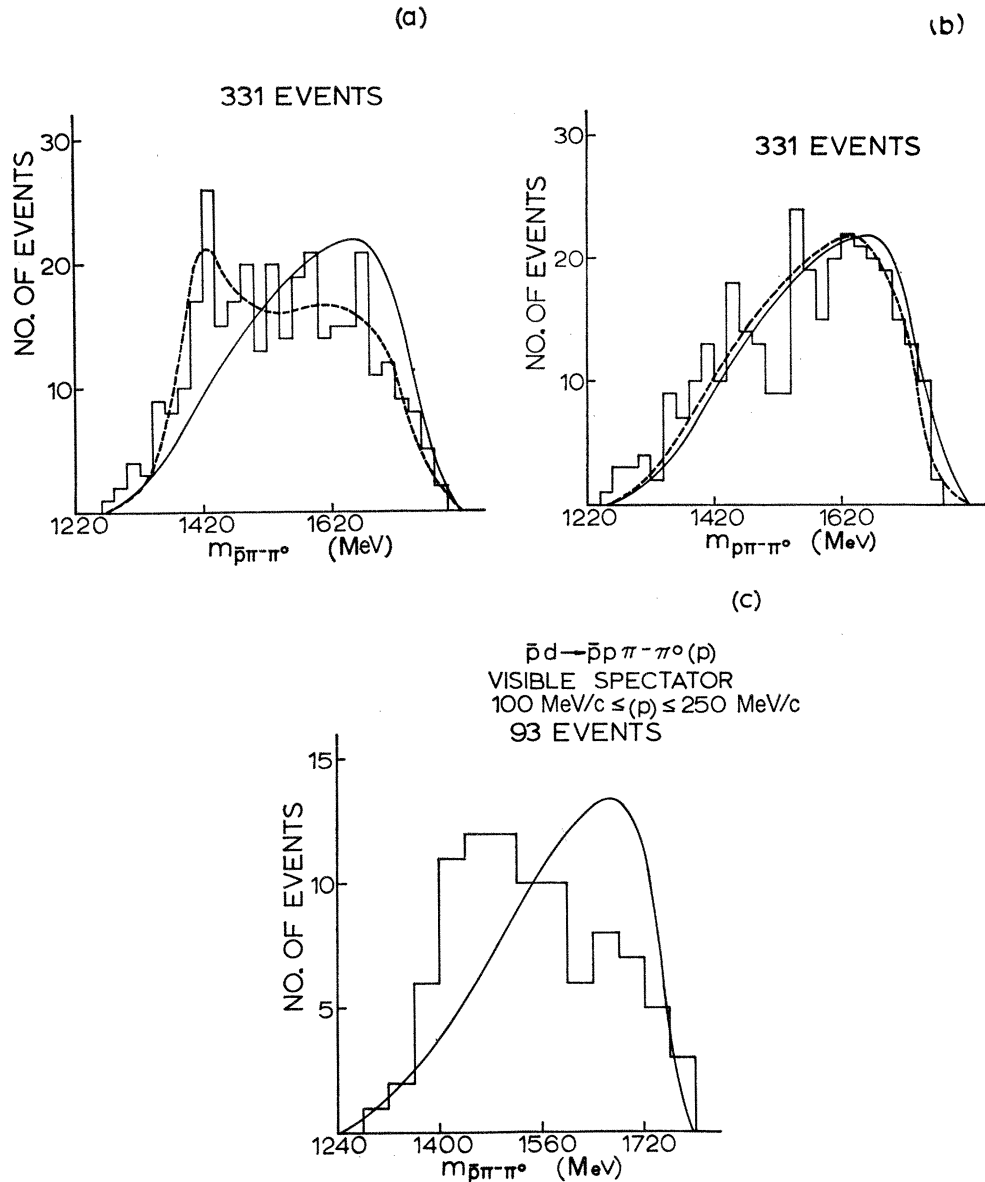


FIG. 19. (a) Effective mass spectrum of the $\bar{p}\pi^-\pi^0$ system in the reaction $\bar{p}n \rightarrow \bar{p}p\pi^-\pi^0$. (b) Effective mass spectrum of the $p\pi^-\pi^0$ system. The solid and dashed curves are in correspondence with those described in Fig. 17. (c) Effective mass of $\bar{p}\pi^-\pi^0$ system for events with visible spectator protons. The solid curve is that in part (a) normalized by 93 events.

likely to contribute to this reaction. They should be compared with Figs. 9(b) and 9(d). Effective mass spectra for the various nucleon- (antinucleon-) pion systems are shown in the histograms of parts (a) and (b) of Figs. 17 and 18. There is clear evidence for the production of $N^*(1238)$ in the $\bar{p}\pi^-$ and $p\pi^0$ systems, but practically none in the $\bar{p}\pi^0$ and $p\pi^+$ systems. After imposing double-resonance cuts on the data in the usual way, namely, $1160 \leq (m_{p\pi}$ and $m_{\bar{p}\pi}) \leq 1300$ MeV, there are 121 candidates for the channel $\bar{p}n \rightarrow \bar{N}^*--N^{*+} \rightarrow \bar{p}\pi^-p\pi^0$ and 62 candidates for the channel $\bar{p}n \rightarrow \bar{N}^*--N^{*0} \rightarrow \bar{p}\pi^0p\pi^-$. Isospin invariance predicts a

ratio of 9 to 4 or 2.25 for these cross sections, while the experimental value is 2.0 ± 0.4 , in good agreement.

The experimental mass spectra of the $\bar{p}\pi^-\pi^0$ and $p\pi^-\pi^0$ systems are shown in the histograms of Fig. 19. The solid and dashed curves are the predictions of a double-scattering model and will be discussed in detail later on. Here again, as in the previous reaction discussed, we note the presence of an enhancement in the low-mass region around 1400 MeV. It is especially apparent in the $\bar{p}\pi^-\pi^0$ system, and it is noteworthy that this system has $T_z = -\frac{3}{2}$, so that this enhancement,

whatever its origin, certainly is not a manifestation of the production of a $T=\frac{3}{2}$ isobar.

Two possible experimental biases which could possibly give rise to this effect were investigated. One of these has been discussed at some length above, namely, the 210 ambiguous events that are consistent with both the $\bar{p}\pi^-p(p)$ and $\bar{p}\pi^-p\pi^0(p)$ hypotheses. However, almost all the $\bar{p}\pi^-\pi^0$ combinations obtained by considering these 210 events as belonging to the latter category were found to have a low effective mass. Hence, inclusion of these events as candidates for this channel would make the observed enhancement larger. Thus, the exclusion of the ambiguous events from the analysis cannot explain the structure at 1400 MeV in the $\bar{p}\pi^-\pi^0$ mass spectrum.

The second possible experimental bias concerned the retrieval of events with invisible spectator protons. This was discussed in the Introduction, where it was pointed out that no differences were found between events with invisible spectator protons and events with visible spectators. Nevertheless, in checking possible biases which could give rise to the structure observed in Fig. 19(a), it was deemed appropriate to plot the $\bar{p}\pi^-\pi^0$ mass spectrum for events with visible spectators only. This distribution is displayed in Fig. 19(c) and demonstrates clearly that the events with visible spectators show the same effect as the total sample.

To investigate whether or not the structure in the three-body mass distributions was a kinematic reflection of some kind, the double-scattering version of the single-pion-exchange model was calculated for this reaction. For this purpose only the upper Feynman diagram of Fig. 16(b) was employed, since its contribution to the cross section is considerably larger than is the contribution of the diagram in Fig. 16(d). The vertex function corresponding to the upper shaded circle of Fig. 16(b) was proportional to the on-the-mass-shell, $T=\frac{3}{2}$, π - p elastic differential scattering cross section, as expressed quantitatively in Eq. (7). The vertex function corresponding to the lower shaded circle is proportional to the on-the-mass-shell charge-exchange scattering cross section for the reaction $\pi^+n \rightarrow \pi^0p$, which is, in turn, related to the reaction $\pi^-p \rightarrow \pi^0n$. Once again the propagator term and all vertex and propagator corrections were collapsed into a single function $F(t)$, constructed so as to reproduce the experimental production distributions. (Here t is the squared four-momentum transfer from the incoming \bar{p} to the outgoing $\bar{p}\pi^-$ system.) The differential scattering cross sections used for the vertex functions were obtained from experimental elastic and charge-exchange scattering data.¹² Finally, the predictions of the double-scattering model were added incoherently to those of Lorentz-invariant phase space, and least-squares fits to the various experimental distributions were made to determine the fraction of each contribution.

The best fit to the data was obtained when the double-

scattering diagram contributed 50% to the cross section with the remaining 50% provided by the phase-space contribution. The absolute uncertainties in these fractions are $\pm 10\%$. The solid curves in Figs. 17–19 represent the predictions of this model. It is noted that all the theoretical proton- (antiproton-) pion effective mass spectra, as well as the virtual scattering angular distributions, are in good agreement with the experimental data (Figs. 17 and 18). However, as seen in Fig. 19(a), the prediction of this model (solid curve) fails to account for the structure in the low-mass region of the $\bar{p}\pi^-\pi^0$ mass spectrum. Moreover, the inclusion in the model of the second Feynman diagram of Fig. 16(d) was found to have no effect on the predicted three-body mass spectrum. In fact, the shapes of the $\bar{p}\pi^-\pi^0$ mass spectrum obtained by using either of the Feynman diagrams alone in Fig. 16 were quite similar. In addition, each of these was quite similar to the prediction of three-out-of-four-body Lorentz-invariant phase space, except that the phase-space prediction falls somewhat more rapidly in the low-mass region.

To account for the structure, a third amplitude was added incoherently to the previous two. This amplitude described the production of an N^* state near 1400 MeV which decayed into $N^*(1238)\pi^0$ according to the scheme $\bar{p}n \rightarrow \bar{N}^{*--}(1400)p \rightarrow \bar{N}^{*--}(1238)\pi^0p \rightarrow \bar{p}\pi^-\pi^0p$. All decay angular distributions were assumed to be isotropic in the rest frame of the decaying particle, and the squared four-momentum transfer distribution to the $N^*(1400)$ system was chosen to duplicate the corresponding experimental distribution for events with $1380 \leq m_{\bar{p}\pi^-\pi^0} \leq 1480$ MeV. The dashed curves in Figs. 17 and 19 represent the predictions of the model modified so as to give the best fit to the data. [In Fig. 17(c) the dashed and solid curves are identical.] They correspond to an incoherent sum of the following contributions: 50% double-scattering model [Fig. 16(b)], 25% $N^*(1400)$ production, and 25% Lorentz-invariant phase space with absolute uncertainties of 7–10%. The mass and width of the $N^*(1400)$ system corresponding to this best fit were 1400 and 80 MeV, in good agreement with those discussed in Sec. IV in connection with the reaction $\bar{p}n \rightarrow \bar{p}n\pi^+\pi^-$.

A fit of the form $d\sigma/dt = Ae^{-bt}$ was made to the experimental t distribution over a range $0.08 \leq t \leq 0.20$ for events in the $N^*(1400)$ region, defined as above to be $1380 \leq M_{\bar{p}\pi^-\pi^0} \leq 1480$ MeV. As usual, t in the above equation is the square of the four-momentum transfer from the incoming \bar{p} to the outgoing system of interest—here, the $\bar{p}\pi^-\pi^0$ system. The slope b was found to have a value 6.2 ± 11 (GeV/ c^2)⁻². The large error resulted from the extremely small sample of events remaining after the various cuts were made.

In connection with the possible presence of a $T=\frac{3}{2}$ resonant state with an $N\pi\pi$ decay mode, the absence of very pronounced structure in the $p\pi^-\pi^0$ mass spectrum [Fig. 19(b)] was explained, at least in part, by

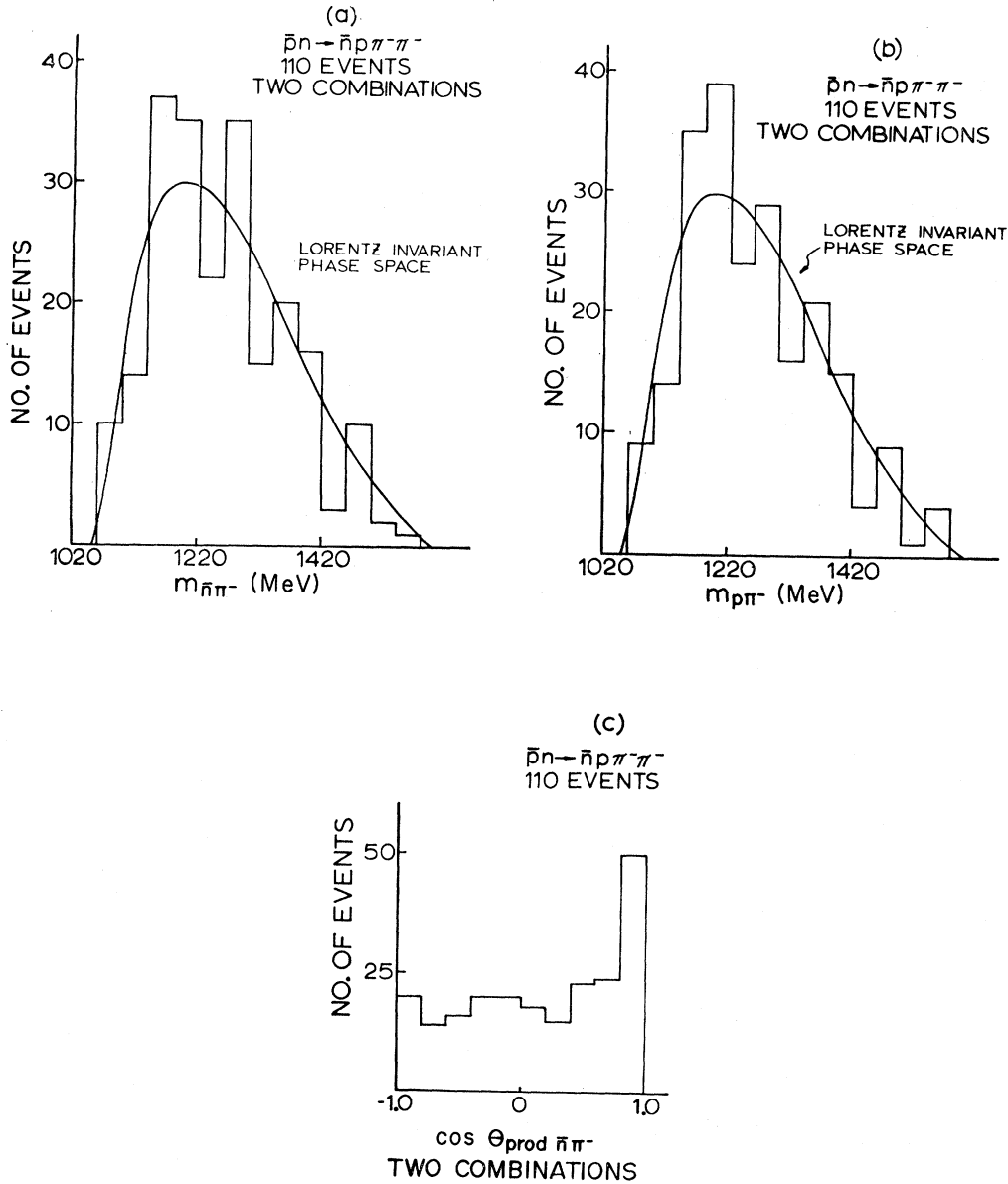


FIG. 20. (a) Effective mass distribution of the $\bar{n}\pi^-$ system from the reaction $\bar{p}d \rightarrow \bar{n}p\pi^-\pi^- (p)$. (b) Effective mass distribution of the $p\pi^-$ system from that reaction. The smooth curves in (a) and (b) are the prediction of Lorentz-invariant phase space. (c) Center-of-mass production angular distribution of the $n\pi^-$ system.

isospin conservation, which predicts relative intensities of $\frac{3}{4}:\frac{1}{4}$ for the reactions $\bar{p}n \rightarrow \bar{N}^*(1400)p$ and $\bar{p}n \rightarrow \bar{p}N^*(1400)$, respectively. If, in addition, the decay mode $N^*(1400) \rightarrow N^*(1238)\pi$ is assumed, the ratio \bar{N}^*/N^* is 35/17 for the final state $\bar{p}p\pi^-\pi^0$. The small statistics and large background prevent further meaningful conclusions.

VI. REACTION $\bar{p}n \rightarrow \bar{n}p\pi^-\pi^-$

This experiment yielded 170 events satisfying the hypothesis $\bar{p}d \rightarrow \bar{n}p\pi^-\pi^-p$. By regarding the slower proton as the spectator and accepting only events with

spectators of momentum less than 250 MeV/c, the sample was reduced to 110 events. This corresponds to a cross section for the reaction $\bar{p}n \rightarrow \bar{n}p\pi^-\pi^- (p)$ of 0.30 ± 0.04 mb.

Because of the limited statistics, detailed analysis of this channel was not attempted. However, some insight into the dynamics of this channel was obtained by examining several relevant distributions. The $\bar{n}\pi^-$ and $p\pi^-$ effective mass distributions are shown in Figs. 20(a) and 20(b). The production angular distribution of the $\bar{n}\pi^-$ system is shown in Fig. 20(c). There, θ_{prod} is the angle between the incoming \bar{p} and the outgoing

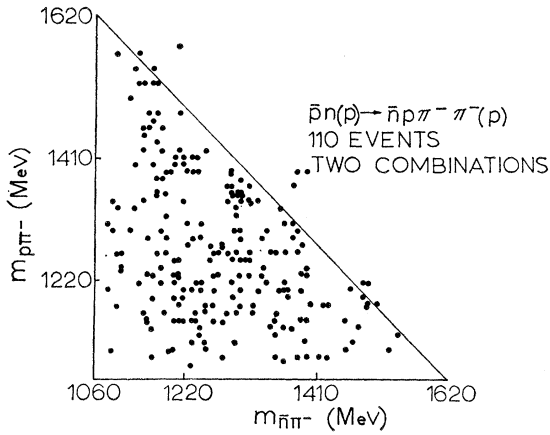


FIG. 21. Scatter plot of $m_{p\pi^-}$ versus $m_{\bar{n}\pi^-}$ for the reaction $\bar{p}n \rightarrow \bar{n}p\pi^-\pi^-$. There are two combinations per event.

$\bar{p}\pi^-$ system in the $\bar{p}n$ center-of-mass frame. Because of the two negative pions in the final state of this reaction, each event is plotted twice in Fig. 20. The solid curves in Figs. 20(a) and 20(b) are the phase-space predictions. There is some tendency for the mass distributions to peak in the neighborhood of the $N^*(1238)$. However, the process appears to be considerably less peripheral than the other channels considered in this work. In Fig. 21 is a scatter plot of the effective $\bar{n}\pi^-$ mass versus the effective $p\pi^-$ mass. There is no evidence for double-isobar production.

VII. CONCLUSIONS AND SUMMARY

Three double-pion production reactions in antiproton-neutron collisions at 2.8 GeV/c have been discussed. In the reactions $\bar{p}n \rightarrow \bar{p}n\pi^+\pi^-$ and $\bar{p}n \rightarrow \bar{p}p\pi^-\pi^0$, there is evidence for the production of $N^*(1238)$ isobars. Attempts to use the absorptive single-pion-exchange model to explain the dynamics of the quasi-two-body reactions (F) and (G), $\bar{p}n \rightarrow \bar{N}^*N^* \rightarrow \bar{p}n\pi^+\pi^-$, failed in most respects. Of particular interest in this context was the comparison of these reactions with the reaction $p\bar{p} \rightarrow N^*N^* \rightarrow p\bar{p}\pi^+\pi^-$. This latter reaction proved experimentally to be more peripheral than the two former reactions, whereas the absorptive model predicted just the opposite.

The double-scattering model fared somewhat better. Although this model did not attempt to predict production angular distributions (or, correspondingly, squared four-momentum distributions), it succeeded in reproducing both two-body mass spectra and decay angular distributions in the reactions $\bar{p}n \rightarrow \bar{p}n\pi^+\pi^-$, $\bar{p}n \rightarrow \bar{p}p\pi^-\pi^0$, and $p\bar{p} \rightarrow p\bar{p}\pi^+\pi^-$. Because of the form of the vertex functions in this model, it was not necessary to restrict the analysis to isobar events alone.

In the $\bar{p}n$ reactions, discrepancies were observed in the nucleon- (antinucleon-) dipion three-body mass spectra. In all cases these discrepancies were removed by assuming the production of N^* states around 1400 MeV. The additional amplitudes necessary to describe this production did not, moreover, affect the agreement between the theoretical predictions and the data in those areas for which such production was not required, namely, the two-body mass and angular distributions. On the other hand, in no case were the experimentally determined parameters of the observed three-body effect in good agreement with those of the Roper resonance. In fact, the observation of this effect in a $T_z = -\frac{3}{2}$ mass spectrum precludes its identification with that resonance.

Thus, we conclude that the data in this experiment cannot be entirely explained by single-pion-exchange models in which pairs of nucleon- (antinucleon-) pion systems are produced. Addition of spin- $\frac{1}{2}$ $N^*(1400)$ amplitudes to such models does, however, produce good agreement with the data.

ACKNOWLEDGMENTS

We would like to thank the operating crews of the alternating gradient synchrotron and the 20-in. bubble chamber, and our scanning and measuring staff for their cooperation. We also gratefully acknowledge the loan of some scanning and measuring equipment by Brookhaven National Laboratory. We are indebted to J. D. Jackson and G. E. Hite for their comments and discussions of the absorptive single-pion-exchange model, and to D. K. Robinson for his help with the $p\bar{p}$ data. We also thank Dr. H. W. K. Hopkins for his assistance in the early stages of this experiment.